A Phenomenological Model of a Downdraft Biomass Gasifier Flexible to the Feedstock Composition and the Reactor Design

Michela Costa [1,*], Maurizio La Villetta [2], Daniele Piazzullo [1] and Domenico Cirillo [2]

[1] Istituto di Scienze e Tecnologie per l'Energia e la Mobilità Sostenibili Motori, CNR, Viale Marconi, 4, 80125 Naples, Italy; daniele.piazzullo@stems.cnr.it
[2] Research & Development Department, Costruzioni Motori Diesel S.p.A., Via Pacinotti, 2, 81020 San Nicola La Strada, Italy; maurizio.lavilletta@cmdengine.com (M.L.V.); domenico.cirillo@cmdengine.com (D.C.)
* Correspondence: michela.costa@stems.cnr.it

Abstract: The development of a one-dimensional (1D) phenomenological model for biomass gasification in downdraft reactors is presented in this study; the model was developed with the aim of highlighting the main advantages and limits related to feedstocks that are different from woodchip, such as hydro-char derived from the hydrothermal carbonization of green waste, or a mix of olive pomace and sawdust. An experimental validation of the model is performed. The numerically evaluated temperature evolution along the reactor gasifier is found to be in agreement with locally measured values for all the considered biomasses. The model captures the pressure drop along the reactor axis, despite an underestimation with respect to the performed measurements. The producer gas composition resulting from the numerical model at the exit section is in quite good agreement with gas-chromatograph analyses (12% maximum error for CO and CO_2 species), although the model predicts lower methane and hydrogen content in the syngas than the measurements show. Parametric analyses highlight that lower degrees of porosity enhance the pressure drop along the reactor axis, moving the zones characterized by the occurrence of the combustion and gasification phases towards the bottom. An increase in the biomass moisture content is associated with a delayed evolution of the temperature profile. The high energy expenditure in the evaporation phase occurs at the expense of the produced hydrogen and methane in the subsequent phases.

Keywords: biomass gasification; syngas; phenomenological model; downdraft; hydro-char

1. Introduction

The current energy system is witnessing an unprecedented transformation, with a general shift of the energy production paradigm from fossil-based to renewable sources [1,2]. The bioeconomy uses renewable natural capital to holistically transform and manage land, food, health and industrial systems with the goal of achieving sustainable wellbeing. The exploitation of residual agricultural biomass, including livestock waste or sewage sludge, is a viable route, which is today widely considered for sustainable energy production in both industrialized and developing countries.

Bioenergy routes include biological and thermochemical treatments of biological resources. Among the different thermochemical paths for biomass utilization, gasification is currently one of the most valuable options [3]. It consists of biomass conversion via partial oxidation reactions into a synthetic gas (syngas or producer gas) that is mainly composed of hydrogen (H_2), methane (CH_4), carbon monoxide (CO), carbon dioxide (CO_2) and water vapor (H_2O), which can be exploited for cogenerative purposes with a low environmental footprint.

However, existing difficulties harm the widespread deployment of energy systems based on biomass gasification, these being closely related to the large variability (mostly particle size, moisture and ash content) of the materials to be processed [4], which in turn

results in a highly variable quality of the produced syngas [5], as well as the co-production of condensable organic compounds (tar) that may cause reactor blockages [6].

In this context, numerical modelling may be a useful tool for a better comprehension of the underlying physical and chemical mechanisms, and hence for the design of new gasification systems or the development of proper control strategies for existing units [7]. Numerical analyses and optimization can allow significant improvements in the whole conversion process [8]. Within the scientific literature, thermodynamic equilibrium models are the most followed numerical approaches, as they are characterized by high simplicity and easily achievable solutions. They release an ideal syngas yield that is based on the stringent hypotheses of infinite biomass residence time within the reactor, and independency of the conversion process from the design features of this reactor [9]. On the opposite side, with respect to model complexity, Computational Fluid Dynamic (CFD) models can be proposed to characterize, in detail, such a complex process, thus providing a very accurate description of the thermochemical process, which is, however, counterbalanced by long computational times [10]. In between, one-dimensional (1D) phenomenological models may represent a good compromise due to their simplicity and moderate computational time to obtain a reliable prediction of the syngas composition and of the thermodynamic field inside the reactor. They consider both the chemical reaction kinetics and information relevant to the fluid dynamics of the reactor, for given operating conditions and feedstock features.

Among the state-of-the-art of phenomenological 1D approaches applied for biomass gasification in downdraft gasifiers, Giltrap et al. [11] predicted the composition of the producer gas from wood biomasses under steady-state operation, employing the reduction zone kinetics rates as derived by Wang and Kinoshita [12]. Di Blasi [13] proposed a 1D phenomenological model for lignocellulosic biomass gasification in a stratified downdraft gasifier, including the reactions of the consecutive processes of drying, pyrolysis, combustion and gasification of char, combustion of the released volatiles and tar cracking.

Sharma [14] presented a phenomenological model for rubber wood gasification in which the reduction zone was modelled using a finite reaction rate, while the pyro-oxidation zone was modelled considering a thermodynamic equilibrium approach. However, char combustion in the pyro-oxidation zone and the formation of methane were not described. Tinaut et al. [15] studied the effects of different sizes of pine bark biomass and different air superficial velocity through the development of a steady 1D model of biomass gasification, while Umeki et al. [16] studied the effects of high-temperature steam as gasifying agent through a validated 1D two-fluid model. Simone et al. [17] developed a phenomenological 1D model to help the interpretation of experimental results achieved in a pilot scale throated downdraft gasifier operated with woody residues as feedstock. Patra et al. [18] developed a comprehensive 1D combined transport and kinetics model operating under unsteady state conditions for the gasification of wood, validated against experimental data in terms of biomass consumption rate, producer gas flow rate and gas composition. A four-zone kinetic model for a downdraft gasifier was developed by Salem et al. [19], in which the gasification products from rubber wood were determined through an approach that finds the optimum length of the reduction zone.

The above, to the best of authors' knowledge, is the state-of-the-art of phenomenological 1D approaches applied to simulate the gasification in the downdraft reactors of only wooden biomasses. The current shift in interest towards thermochemical treatments of other kinds of biological feedstocks, such as agricultural, green wastes or crop residuals, needs more flexible approaches. Examples include olive pomace from the olive oil extraction process, or hydro-char derived from hydro-thermal carbonization (HTC) of green waste, the latter being the most exploited for fertilization or as char in combustion devices, such as those considered in this study.

Therefore, a stationary 1D phenomenological model of biomass gasification in a fixed bed downdraft gasifier is here presented, validated with respect to data coming from a dedicated experimental campaign accounting for two types of woodchip, hydro-char derived from green waste HTC and a mix of olive pomace and sawdust.

The main aim of the work is to highlight advantages and limits of the here-developed model when applied to simulate the thermochemical conversion of feedstocks of non-woody biomasses, by bringing to light the main shortcomings that arise when considering materials characterized by high calorific values and high ash contents.

Biomass characterizations are performed according to standard methods, and measured values of porosity of the actual feedstock are used to set the input parameters of the model. Numerical results are compared with experimental data that are relevant to the temperature and pressure evolution at some points along the reactor axis, and syngas composition as derived from sampling and gas chromatograph analyses.

Lastly, parametric analyses are performed to highlight the effects of variables, such as the biomass moisture content, the equivalence ratio (ER) and the porosity of the bed, on the conversion efficiency.

2. Materials and Methods

The model proposed in this study is developed within the MATLAB environment and is validated using experimental data from gasification of two types of woodchip, hydro-char derived from green waste HTC and a mix of olive pomace and sawdust in a downdraft reactor being part of a real micro-cogeneration system.

2.1. One-Dimensional Phenomenological Approach

The gasification process in a downdraft gasifier is modelled by means of a 1D schematization along the reactor axis, solving the equations of mass and energy balance for porous media to each differential volume ΔV that is treated as a Continuous Stirred Tank Reactor (CSTR), whose diameter is equal to the local reactor diameter D_{react} with height Δz along the gasifier axis. The adopted approach is aligned to that of Tartarelli and Seggiani [20].

Turbulence is not treated formally but is implicitly accounted for through correlations of the actual heat/mass transfer coefficients. The fed particles are considered to be of spherical shape while the porosity of the bed, ε, is assumed to be constant along the gasifier, although they are imposed as though derived from measurements taken on the real feedstock.

Modelling of sub-processes includes:

- Moisture (M) evaporation by a 1st order kinetic equation;
- Biomass/residual material (W) devolatilization described by one-step global reaction;
- Char (C) gasification reactions;
- Combustion of volatile species.

The related reactions are listed in Table 1.

Table 1. Reactions occurring in a downdraft gasifier.

Reaction	Reaction Name
$Biomass_{wet} \rightarrow Biomass_{dry} + H_2O_{vapour}$	Drying
$Biomass_{dry} \rightarrow Char + Volatiles\ (Gas + Tar)$	Devolatilization
Heterogeneous Reactions	
$C + ER \cdot O_2(g) \rightarrow 2(1 - ER) \cdot CO + (2 \cdot ER - 1)\ CO_2$	Oxidation
$C + CO_2(g) \rightarrow 2CO$	Boudouard Reaction
$C + H_2O(g) \rightarrow CO + H_2$	(Water/gas heterogeneous reaction)
$C + 2H_2(g) \rightarrow CH_4$	(Methane formation reaction)
Homogeneous Reactions	
$CO + H_2O(g) \leftrightarrow CO_2 + H_2$	(Water/gas shift reaction)
$Tar + O_2 \rightarrow CO + H_2O$	
$Tar + H_2O \rightarrow CO + H_2O$	(Tar reforming)
$Tar \rightarrow CO + CO2 + CH_4 + H_2$	(Tar cracking)
$CH_4 + 2O_2 \rightarrow CO + 2H_2O$	
$CH_4 + H_2O \leftrightarrow CO + 3H_2$	(Methane reforming reaction)
$CO + 0.5O_2 \rightarrow CO_2$	
$H_2 + 0.5O_2 \rightarrow H_2O$	

The solid phase is characterized in terms of partial bed densities ρ_i (kg/m^3 bed volume), where i = M, W_{daf}, (C) and ashes (A), by the solid velocity U_S (m/s), temperature T_S (K) and pressure P_S (Pa).

Similarly, the gas phase is described in terms of the partial densities ρ_j (kg/m^3 gas volume) for j = O_2, N_2, H_2O, CO_2, CO, H_2, CH_4, H_2S, TAR, gas velocity U_G (m/s), temperature T_G (K) and pressure P_G (Pa).

The equations to be solved are the following:

Ideal gas law

$$\sum_j \rho_j/M_j = P_G/(R \cdot T_G) \quad j = O_2, N_2, H_2O, CO_2, CO, H_2, CH_4, H_2S, TAR \tag{1}$$

where the left-hand side represents the total gaseous density obtained as a sum of the ratios between the partial densities ρ_j and the molecular weight M_j of the nine considered gaseous species, and R is the gas universal constant.

Mass conservation of the solid-phase species

$$\textbf{Biomass:} \ \partial(U_S \cdot \rho_W)/\partial z = -R_{dev} \tag{2}$$

$$\textbf{Moisture:} \ \partial(U_S \cdot \rho_M)/\partial z = -R_{dry} \tag{3}$$

$$\textbf{Char:} \ \partial(U_S \cdot \rho_C)/\partial z = \alpha_2 \cdot (M_C/M_W) \cdot R_{dev} - R_{S1} - R_{S2} - R_{S3} - R_{S4} \tag{4}$$

$$\textbf{Ash:} \ \partial(U_S \cdot \rho_A)/\partial z = 0 \tag{5}$$

where the source terms on the right-hand side represent the kinetic rates for the drying, devolatilization and the four char heterogeneous reactions; the latter is described in more detail in the subsequent section.

Mass conservation of the gas-phase species

$$\partial(\varepsilon \cdot U_G \cdot \rho_{O_2})/\partial z = -M_{O_2} \cdot [0.5 \cdot R_{G1} + 0.5 \cdot R_{G2} + 2 \cdot R_{G3} + (m/2 + n/4) \cdot R_{G4}] - 0.5 \cdot (M_{O_2}/M_C) \cdot R_{S1} \tag{6}$$

$$\partial(\varepsilon \cdot U_G \cdot \rho_{N_2})/\partial z = -g \cdot (M_{N_2}/M_W) \cdot R_{dev} \tag{7}$$

$$\partial(\varepsilon \cdot U_G \cdot \rho_{H_2O})/\partial z = R_{dry} + d \cdot (M_{H_2O}/M_W) \cdot R_{dev} + M_{H_2O} \cdot [R_{G2} + 2 \cdot R_{G3} + (n/2) \cdot R_{G4} - R_{WG}] - (M_{H_2O}/M_C) \cdot R_{S4} \tag{8}$$

$$\partial(\varepsilon \cdot U_G \cdot \rho_{CO_2})/\partial z = e \cdot (M_{CO_2}/M_W) \cdot R_{dev} + M_{CO_2} \cdot [R_{G1} + R_{G3} + m \cdot R_{G4} + R_{WG}] - (M_{CO_2}/M_C) \cdot R_{S2} \tag{9}$$

$$\partial(\varepsilon \cdot U_G \cdot \rho_{CO})/\partial z = c \cdot (M_{CO}/M_W) \cdot R_{dev} - M_{CO} \cdot (R_{G1} + R_{WG}) + (M_{CO}/M_C) \cdot (R_{S1} + 2 \cdot R_{S2} + R_{S4}) \tag{10}$$

$$\partial(\varepsilon \cdot U_G \cdot \rho_{H_2})/\partial z = a \cdot (M_{H_2}/M_W) \cdot R_{dev} + M_{H_2} \cdot (R_{WG} - R_{G2}) + (M_{H_2}/M_C) \cdot (-2 \cdot R_{S3} + R_{S4}) \tag{11}$$

$$\partial(\varepsilon \cdot U_G \cdot \rho_{CH_4})/\partial z = b \cdot (M_{CH_4}/M_W) \cdot R_{dev} - M_{CH_4} \cdot R_{G3} + (M_{CH_4}/M_C) \cdot R_{S3} \tag{12}$$

$$\partial(\varepsilon \cdot U_G \cdot \rho_{H_2S})/\partial z = f \cdot (M_{H_2S}/M_W) \cdot R_{dev} \tag{13}$$

$$\partial(\varepsilon \cdot U_G \cdot \rho_{TAR})/\partial z = (M_{TAR}/M_W) \cdot R_{dev} - M_{TAR} \cdot R_{G4} \tag{14}$$

where the right-hand side contains the stoichiometric coefficients (a, b, c, d, e, f, g, m, n) of the reaction, obtained from the balance equations of the products' yield, and the reaction rates for the drying, devolatilization, the four char heterogeneous reactions and the five homogeneous reactions. All of these will be more thoroughly introduced later in this section.

Energy balances for the solid and gas phases

$$\partial(U_S \cdot \rho_S \cdot H_S)/\partial z = -Q_{SG} - Q_{SW} + (-\Delta H_{dry}) \cdot R_{dry} + \sum_{j=1:4} (-\Delta H_{RSj}) \cdot R_{Sj} \tag{15}$$

$$\partial(\varepsilon \cdot U_G \cdot \rho_G \cdot H_G)/\partial z = +Q_{SG} - Q_{GW} + \sum_{j=1:5} (-\Delta H_{RGj}) \cdot R_{Gj} \tag{16}$$

where:

- $H_S = c_{pS} \cdot (T_S - 298.15)$;

- $H_G = c_{pG} \cdot (T_G - 298.15)$;
- $Q_{SW} = (4 \cdot h_{SW} / D_{react}) \cdot (T_S - T_{wall})$;
- $Q_{GW} = (4 \cdot h_{GW} / D_{react}) \cdot (T_G - T_{wall})$;
- $Q_{SG} = h_{SG} \cdot A_{SG} \cdot (T_S - T_G)$;
- $A_{SG} = 6 \cdot (1 - \varepsilon) / d_p$.

where the reactor diameter D_{react} is assumed to vary along the axis according to the geometrical measurement taken on the real system. This is made to implicitly relate the relative position of the drying, pyrolysis, oxidation and reduction zones with the throat location.

In the previous equations, H_S and H_G are the solid and gaseous phases enthalpies, $h_{SW} - h_{GW} - h_{SG}$ and $Q_{SW} - Q_{GW} - Q_{SG}$, respectively, represent the heat transfer coefficients (W/m^2K) and the specific heat fluxes between the gasifier wall and the solid phase (SW), the solid walls and the gaseous phase (GW) and between each phase (SG). The specific heat fluxes $h_{SW} - h_{GW}$ are expressed referring to the hydraulic radius, which is defined as the cross-sectional area of the reactor divided by the perimeter.

The specific heats, at constant pressure, c_p, are evaluated through polynomial expression as a function of temperature, as reported by Knacke et al. [21]. ΔH_i are the reaction heats adopted, which are better described in the next section, and are derived from the paper published by Hobbs et al. [22] considering spherical parcels of diameter d_P, while A_{SG} is the specific surface area of the particle, whose unit is m^2/m^3_{bed} [20].

The equation relative to the heat flux between the solid and the gaseous phase, Q_{sg}, is implemented from [13], while the convective heat transfer coefficient h_{sg} (W/m^2K) is derived from the Nusselt number; the latter expresses the weight of the convective process of heat transfer over the conductive one within the gaseous mixture. The chosen correlation for the Nusselt as a function of the Reynolds and Prandtl numbers is relevant to a flow investing a cylinder, as this is a condition that can better reflect the real conversion process occurring in the reactor, where the gasifying agent hits particles of solid material undergoing a progressive change of composition and morphology:

$$Nu = 0.683 \cdot Re^{0.466} \cdot Pr^{1.3} \tag{17}$$

where Equation (17) assumes a "local" validity in the developed model, since the Reynolds and Prandtl numbers are calculated cell by cell along the vertical gasifier direction. In the considered operative cases, the range of variation of Reynolds is Re = 200–400, while for the Prandtl number it is Pr = 0.7–0.9.

Regarding the mathematical approach, the model is solved by dividing the system of differential-algebraic equations into two sub-systems: the first is composed by the ordinary differential Equations (ODE) (1)–(16), solved through the algorithm ODE15s (Gear's method), which is suitable for the solution of stiff problems as the integration step can be reduced when the gradient of variables sharply increases. The other is a non-linear algebraic system conducted according to the following equations:

$$T_S = H_S / (\rho_S \cdot c_{pS} \cdot U_S) \tag{18}$$

$$T_G = H_G / (\rho_G \cdot c_{pG} \cdot U_G) \tag{19}$$

the temperatures of the gaseous and solid phases are evaluated from the enthalpy values achieved through Equations (15) and (16);

$$(\rho_{N_2} / M_{N_2}) = P / (R \cdot T_G) - \sum_i \rho_{Gi} / M_i \quad i = O_2, H_2O, CO_2, CO, H_2, CH_4, H_2S, TAR \tag{20}$$

the nitrogen density is obtained by difference with respect to the densities of the other gaseous species, these solved through Equations (6)–(14);

$$U_G = (U_G \cdot \rho_G) / (\sum_I \cdot \rho_{Gi}) \quad i = O_2, N_2, H_2O, CO_2, CO, H_2, CH_4, H_2S, TAR \tag{21}$$

$$U_S = \text{constant} \tag{22}$$

$$dP/dz = -(150\mu_G \cdot (1-\varepsilon)^2)/(d_{p0}{}^2 \cdot \varepsilon^3) \cdot U_G - (1.75 \cdot \rho_G \cdot (1-\varepsilon))/(d_{p0} \cdot \varepsilon^3) \cdot U_G{}^2 \tag{23}$$

the velocity of the gaseous phase is obtained by solving Equations (6)–(14), while the velocity of the solid phase is assumed as constant. The pressure variation along the reactor axis is obtained by solving Equation (23), as proposed by Giltrap et al. [11], as a function of the gaseous density, the particle diameter, the gaseous velocity, the bed porosity and the fluid viscosity μ_G. This equation system is solved through the Newton–Raphson algorithm.

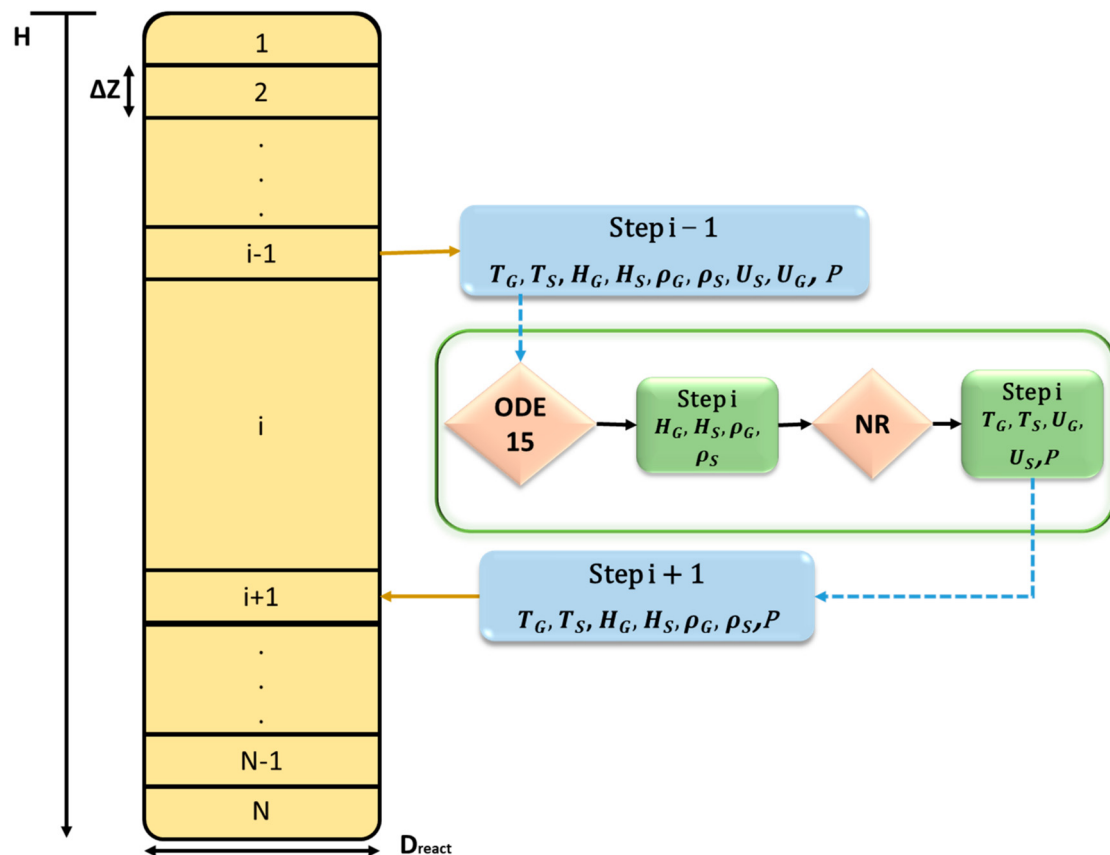A schematization of the whole approach is reported in Figure 1.

Figure 1. Reactor schematization for the mathematical approach.

2.2. Adopted Kinetic Rates

Drying, devolatilization and homogenous reaction kinetics are derived from studies that are relevant to wood gasification but also suitable for biomasses of different compositions. The reactions and reaction rates adopted in the present model are hereafter described.

During the drying phase, the wet biomass is heated up by exploiting the hot gases coming from the lower zones of combustion/gasification, releasing its moisture content. The kinetic rate R_{dry} is described according to a first order kinetic approach, thus depending upon the local temperature value according to the Arrhenius equation [23]:

$$R_{dry} = \rho_{H_2O} \cdot A_{H_2O} \cdot \exp(-E_{H_2O}/(R \cdot T_S)) \tag{24}$$

where A_{H_2O} is the pre-exponential factor equal to 5.56×10^6 s^{-1} and E_{H_2O} is the activation energy equal to 8.79×10^4 J/mol.

As concerns biomass pyrolysis, many researchers [24–31] describe this process through a two-stage parallel reaction model. The biomass first undergoes a primary thermal degradation producing gases, tar and char. The primary pyrolysis products, condensable
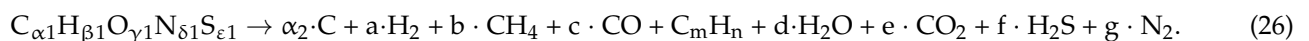
and non-condensable vapors, and char are then considered to undergo secondary reactions in the presence of the gasification agent, thus forming additional amounts of gaseous compounds [32]. In the present work, devolatilization of biomass is described by a first-order one-step global reaction estimated by an Arrhenius expression, as also proposed by Teislev [33]. Five splitting factors for char, hydrogen, methane, carbon monoxide and water vapor are introduced to determinate the stoichiometry of the pyrolysis reaction.

The kinetic rate is modelled as:

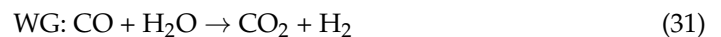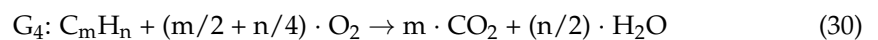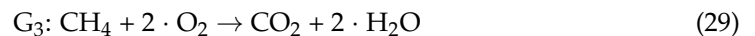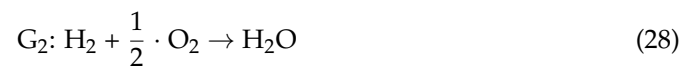$$R_{dev} = \rho_W \cdot K_0 \cdot \exp(-E/(R \cdot T_S)) \tag{25}$$

where $K_0 = 2 \times 10^4 \text{ s}^{-1}$ and $E/R = 8467$ K.

This term appears at the right-hand side of each of the species mass balance equation, multiplied by a proper coefficient derived from the general devolatilization reaction:

$$C_{\alpha1}H_{\beta1}O_{\gamma1}N_{\delta1}S_{\varepsilon1} \rightarrow \alpha_2 \cdot C + a \cdot H_2 + b \cdot CH_4 + c \cdot CO + C_mH_n + d \cdot H_2O + e \cdot CO_2 + f \cdot H_2S + g \cdot N_2. \tag{26}$$

In Equation (26), α_2, a, b, c, d, e, f, g, m, n are the stoichiometric coefficients of the reaction, obtained from the balance equations of the products yields [20]. These are better described in the Supplementary Materials.
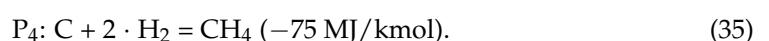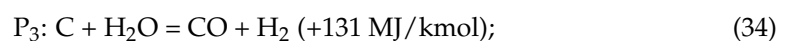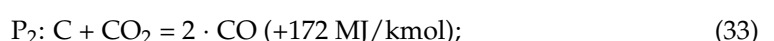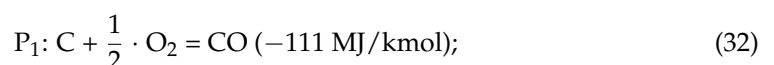
The combustion homogeneous reactions considered in the present model are:

$$G_1: CO + \frac{1}{2} \cdot O_2 \rightarrow CO_2 \tag{27}$$

$$G_2: H_2 + \frac{1}{2} \cdot O_2 \rightarrow H_2O \tag{28}$$

$$G_3: CH_4 + 2 \cdot O_2 \rightarrow CO_2 + 2 \cdot H_2O \tag{29}$$

$$G_4: C_mH_n + (m/2 + n/4) \cdot O_2 \rightarrow m \cdot CO_2 + (n/2) \cdot H_2O \tag{30}$$

$$WG: CO + H_2O \rightarrow CO_2 + H_2 \tag{31}$$

where WG represents the water–gas shift reaction.

Lastly, the heterogeneous reactions, describing the char conversion into volatile compounds, follows the Shell Progressive (SP) approach, where it is assumed that the external char particle diameter remains constant, and equal to dp_0, while the inner core d_c reduces during the gasification reactions.

Char gasification kinetics is modelled with particular attention as its reactivity varies with the degree of conversion and residence time and because it is a slower process than the initial pyrolysis [34,35]. This aspect must be taken into account in the proper design of new gasifiers. In general, there are many publications concerning the gasification kinetics of chars obtained from different types of coal [36,37] or any type of biomass [38,39]. First-order kinetics often holds only for a part of the conversion interval and a more adequate kinetics schematization is needed [40]. Therefore, within the present work, char is assumed as consisting of pure carbon, as the experimental evidence proves that just negligible amounts of hydrogen and oxygen are present, reacting with O_2, CO_2, H_2O and H_2 according to the heterogeneous reactions. These are the following:

$$P_1: C + \frac{1}{2} \cdot O_2 = CO \ (-111 \text{ MJ/kmol}); \tag{32}$$

$$P_2: C + CO_2 = 2 \cdot CO \ (+172 \text{ MJ/kmol}); \tag{33}$$

$$P_3: C + H_2O = CO + H_2 \ (+131 \text{ MJ/kmol}); \tag{34}$$

$$P_4: C + 2 \cdot H_2 = CH_4 \ (-75 \text{ MJ/kmol}). \tag{35}$$

The reaction heats reported in brackets in Equations (32)–(35) state the endothermic (if positive) or exothermic (if negative) nature of each reaction.

The reactions and reaction rates adopted in the present model are summarized in Table 2, where [X] expresses the general species concentration in $kmol/m^3$, while the devolatilization kinetic rates used as the right-hand terms in each of the Equations (6)–(14), and the kinetic constants of the heterogeneous reactions listed in Table 2 are, respectively, reported in Tables S1 and S2 in the Supplementary Materials.

Table 2. Reactions and reaction rates used in the present model.

Drying
Biomass wet → Biomass dry + H_2O vapor [23]
R_{dry} (kg/(s·m^3_{bed})) = ρ_{H_2O}·5.56 × 10^6·exp($-8.79 \times 10^4/(8.31 \cdot T_S)$)
Devolatilization
$C_{\alpha 1}H_{\beta 1}O_{\gamma 1}N_{\delta 1}S_{\varepsilon 1} \rightarrow \alpha_2 \cdot C + a \cdot H_2 + b \cdot CH_4 + c \cdot CO + C_mH_n + d \cdot H_2O + e \cdot CO_2 + f \cdot H_2S + g \cdot N_2$ [33]
R_{dev} (kg/(s·m^3_{bed})) = ρ_W·2 × 10^4·exp($-8467/T_S$)
Homogeneous reactions gas phase
G_1: $CO + \frac{1}{2} O_2 \rightarrow CO_2$ [23]
R_{G1} (kmol/(s·m^3)) = $\varepsilon \cdot k_{G1} \cdot [CO] \cdot [H_2O]^{0.5} \cdot [O_2]^{0.5}$ with $k_{G1} = 1.3 \times 10^{14} \cdot$exp($-62,700/T_G$)
G_2: $H_2 + \frac{1}{2} O_2 \rightarrow H_2O$ [23]
R_{G2} (kmol/(s·m^3)) = $\varepsilon \cdot k_{G2} \cdot [H_2] \cdot [O_2]$ with $k_{G2} = 8.83 \times 10^{11} \cdot$exp($-12,005/T_G$)
G_3: $CH_4 + 2O_2 \rightarrow CO_2 + 2 H_2O$ [23]
R_{G3} (kmol/(s·m^3)) = $\varepsilon \cdot k_{G3} \cdot [CH_4] \cdot [O_2]$ with $k_{G3} = 2.552 \times 10^{17} \cdot$exp($-11,196/T_G$)
G_4: $C_mH_n + (m/2 + n/4) O_2 \rightarrow m CO_2 + n/2 H_2O$ [38]
R_{G4} (kmol/(s·m^3)) = $\varepsilon \cdot k_{G4} \cdot [C_mH_n]^{0.5} \cdot [O_2]$ with $k_{G4} = 1891 \cdot T_G \cdot$exp($-12,200/T_G$)
Water–gas shift reaction
$CO + H_2O \rightarrow H_2 + CO_2$ [13,23]
R_{WG} (kmol/(s·m^3)) = $\varepsilon \cdot k_{WG} \cdot \{[CO] \cdot [H_2O] - [CO_2] \cdot [H_2]/K_{WGeq}\}$
with $k_{WG} = 2.78 \times 10^3 \cdot$exp($-1513/T_G$) $K_{WGeq} = 0.0265 \cdot$exp($-3966/T_G$)
Heterogeneous reactions involving carbon
(P_1): $C + \frac{1}{2} O_2 \rightarrow CO$ [31]
(P_2): $C + CO_2 \rightarrow 2 CO$ [23]
(P_3): $C + H_2O \rightarrow H_2 + CO$ [31]
(P_4): $C + 2 H_2 \rightarrow CH_4$ [23]
R_{SP} (kg$_C$/(s·m^3_{bed})) = $\{\rho_{Gl}/[(1/k_{diff,Gl}) + (1/k_{ash,Gl}) \cdot (1/\xi - 1) + (1/k_{Rp,Gl} \cdot \xi^2)]\} \cdot [M_C/(\upsilon_{Rp,Gl} \cdot M_{Gl})] \cdot A_{SG}$
with Gl = O_2, CO_2, H_2O, H_2. The coefficients k_i are listed in Table S2 in the Supplementary Materials.

2.3. Experimental Characterization of Biomass Gasification System

An experimental investigation is properly performed to characterize the performances of the here-studied downdraft gasifier, belonging to the Combined Heat and Power (CHP) system, called ECO20 X, developed by the Italian company Costruzioni Motori Diesel S.p.a. (C.M.D.) [41], and experimentally characterized in the main thermodynamic variables as a whole plant in ref. [42]. The real gasifier is shown in Figure 2.

Figure 2. Downdraft gasifier developed by the C.M.D. company.

The tested biomasses differ in composition and in shape: woodchip has a consistency and size that is suitable for direct gasification, while preliminary mechanical pre-treatments of briquetting were needed to process both olive pomace and hydro-char. A briquette made of 100% green waste hydro-char was found to sufficiently resist tangential stresses in the reactor without crumbling, while an 85% concentration of sawdust mixed with olive pomace was necessary to ensure the tolerance to the mechanical stresses of the handling and loading processes. Table 3 shows the images of the tested biomasses before and after the briquetting process along with their main physical characteristics. Woodchip is obtained after a mechanical pre-treatment involving a shredding process, which produces an average woodchip length between 10 and 30 mm. On the other hand, briquettes of green waste HTC and mixtures of olive pomace and sawdust have a diameter of 35 mm and a length between 40 and 80 mm.

The degree of porosity ε to be imposed in the numerical model, that affects the conversion rate of the biomass, and hence the residence time of the material in the reactor, was evaluated for each tested biomass by measuring the ratio of the volume occupied by the residual material in a bucket with respect to the volume of the bucket itself. The calculated values derive from an average over five measurements and are reported in Table 3. The difference in the porosity of the hydro-char and olive pomace briquettes is due to the diverse level of resistance of the two materials when compressed, with the hydro-char leading to briquettes remaining more unbroken than those made of olive pomace.

The following experimental data were collected at the plant site for a correct model initialization and validation:

- The biomass/residual material composition, flow rate and chemical features, the latter reported in Table 4 in terms of proximate analysis (expressed in dry basis, d.b.) defined using a LECO CHN-628 analyzer according to the ASTM D5373 procedure, ultimate analysis (expressed in dry-ash free basis, daf) using a TGA 701 LECO thermo-gravimetric analyzer according to the ASTM D5142 procedure, and calorific values—each measurement was performed five times. Table 4 reports the calculated mean values;
- Low-frequency pressure sensors and k-type thermocouples were mounted along the reactor axis, respectively, for the measurement of the gaseous pressure and temperature to be used for the validation of the model results. Table 5 reports the gasifier characteristics, together with the details about the position of each thermocouple and pressure sensor applied.

Syngas samples were collected in bags and analyzed through a gas chromatograph to evaluate the chemical composition of the gaseous fuel produced for each biomass tested. Their composition is reported in Table 6 in terms of mass fractions on a daf basis. The gasification of all the biomasses was performed at an equivalence ratio of 0.3 and considering a biomass mass flowrate of 24 kg/h. It must be said that for the green waste hydro-char, the moisture and the ash contents in the feedstock were found to play a decisive role during the conversion process, as their fusion created agglomerates that hindered a smooth flow across the reactor, undermining the overall efficiency of the experimental plant until the end of the process.

Table 3. Tested biomasses before and after briquetting treatment and assumed degree of porosity in the reactor.

Biomass	As Delivered	After Briquetting	Average Dimensions	Average Density [kg/m^3]	Porosity ε
Woodchip Case 1		-	10–30 mm	860	0.5
Woodchip Case 2		-	10–30 mm	810	0.5
Hydro-char			Length: 40–80 mm. Diameter: 35 mm.	1250	0.55
Olive Pomace			Length: 40–80 mm. Diameter: 35 mm.	808	0.5

Table 4. (a) Proximate analysis, (b) ultimate analysis, (c) heating value for the four biomasses tested.

Parameter	Woodchip Case 1	Woodchip Case 2	Hydro-Char	Olive Pomace
		(a) Proximate analysis		
Initial Moisture	11.2%	15.9%	12.4%	8.4%
Ash (db)	0.56%	0.36%	17.36%	3.72%
Volatile matter (db)	82.89%	78.64%	59.13%	74.34%
Fixed carbon (db)	16.67%	21%	23.51%	21.94%
		(b) Ultimate analysis		
Carbon (daf)	45.5%	44.4%	65.2%	50.2%
Hydrogen (daf)	5.6%	5.2%	6.3%	5.9%
Nitrogen (daf)	0.0%	0.2%	1.3%	0.8%
Oxygen (daf)	48.9%	50.0%	27.2%	43.1%
		(c) Heating value		
High calorific value kJ/kg (daf)	17,068	17,026	26,815	19,654
Lower calorific value kJ/kg (daf)	15,710	16,854	25,457	18,296

Table 5. Real gasifier characteristics.

Characteristic	Value
Maximum Reactor Diameter.	0.21 m
Minimum Reactor Diameter	0.10 m
Gasifier Length	1 m
Equivalence ratio	0.3
1st Thermocouple position	0.06 m
2nd Thermocouple position	0.78 m
3rd Thermocouple position	0.98 m
1st Pressure Sensor position	0.06 m
2nd Pressure Sensor position	0.98 m

**Table 6.** Collected syngas mass fractions on dry basis for the four biomasses tested.

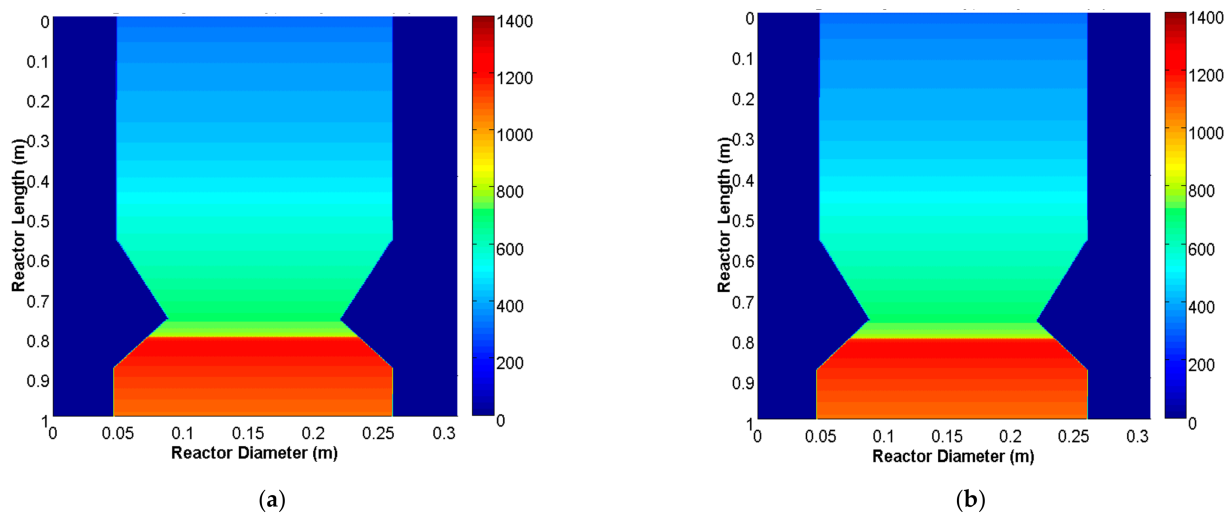| Species	Woodchip Case 1	Woodchip Case 2	Hydro-Char	Olive Pomace
$H_2\%$	1.21	1.65	1.53	1.58
$N_2\%$	61.79	43.2	54.64	45.0
$CO\%$	20.55	26.87	21.45	11.24
$CH_4\%$	1.17	1.09	1.52	3.1
$CO_2\%$	15.29	26.52	17.73	39.08

3. Results

3.1. Model Validation and Results

Figure 3 reports the comparison between the experimental measurements and the numerical profile of the gaseous phase temperature along the reactor axis for the four tested biomasses. The agreement is considered satisfactory, as the results achieved with the numerical model well respect the temperature evolution depicted from the measurement by the thermocouples, proving the versatility of the developed model with the operative condition being tested. In general, after entering the gasifier, the treated biomass heats-up and loses its moisture content. After achieving a complete depletion of the biomass water content, the gaseous temperature rapidly increases due to the activation of the pyrolysis mechanisms in a temperature range between 400 and 700 K. Subsequently, after 800 K, the gasification and combustion reactions take place in both the homogeneous and heterogeneous phases, allowing the gaseous species temperature to rapidly reach a peak at an axial position around the throat. After the peak, the temperature decreases because only ashes remain, and the only reaction that is still present is the water–gas shift reaction. The highest heating value that characterizes the hydro-char is responsible for an anticipated combustion phase with respect to the other cases analyzed, reaching a temperature peak of 1345 K compared to a value of around 1200 K for the other raw materials. This trend is better highlighted in a different visualization of the temperature field in Figure 4 where the temperature iso-surfaces are shown along the reactor geometry, highlighting the zones around the throat where the highest temperatures are reached.

Figure 5 reports the comparison of the pressure evolution along the axis reactor. The measured pressure drop in the reactor is of about 80 mbar for all the cases considered. This trend is reproduced by numerical results, although an underestimation is observed for all the considered conditions. This is mainly an effect that is derived from the employed Shell Progressive (SP) approach, where it is assumed that the external char particle diameter remains constant while the inner core is reduced during the gasification reactions. Therefore, the pressure drop, as described by Equation (23), is underestimated as this effect is not, at this point, considered.
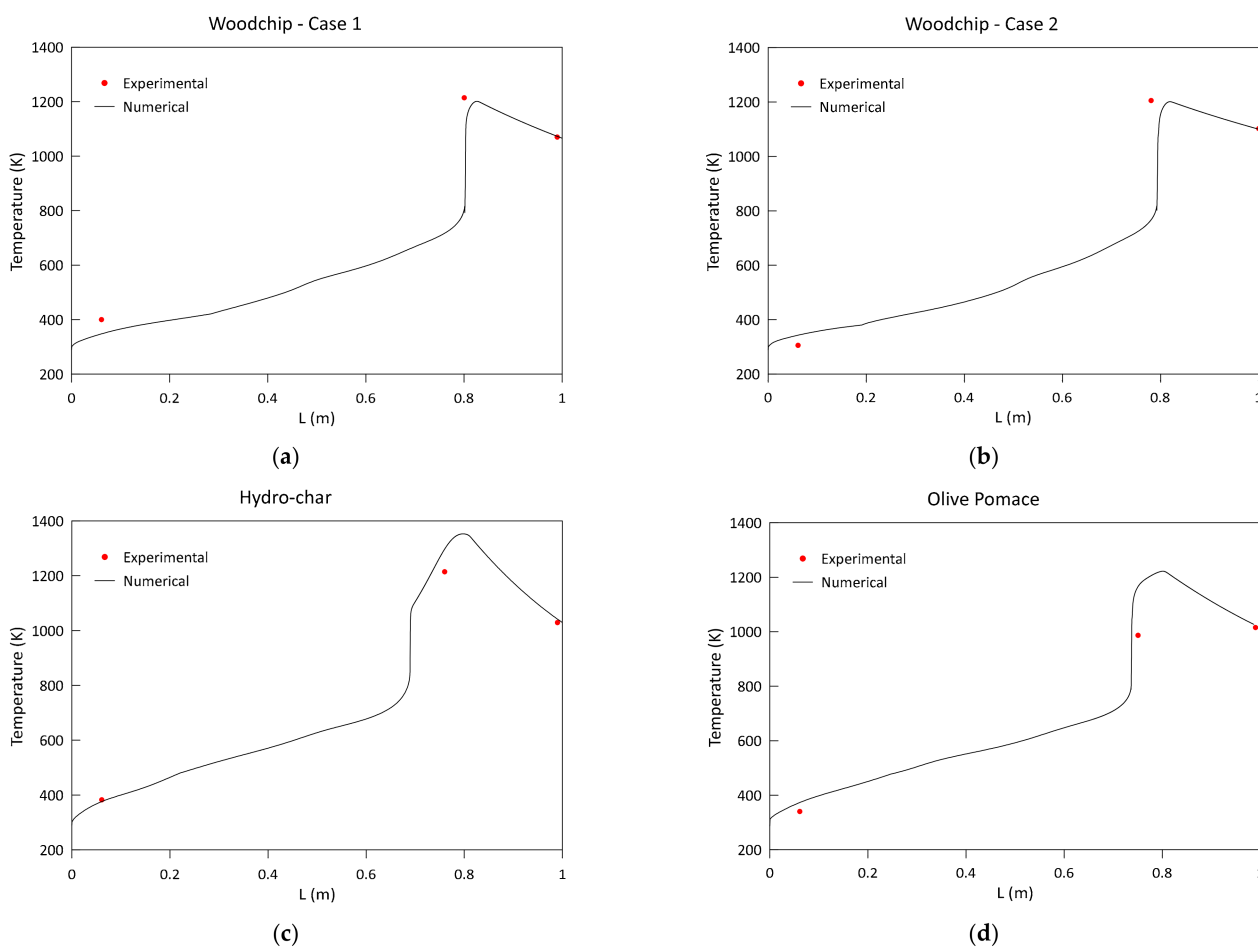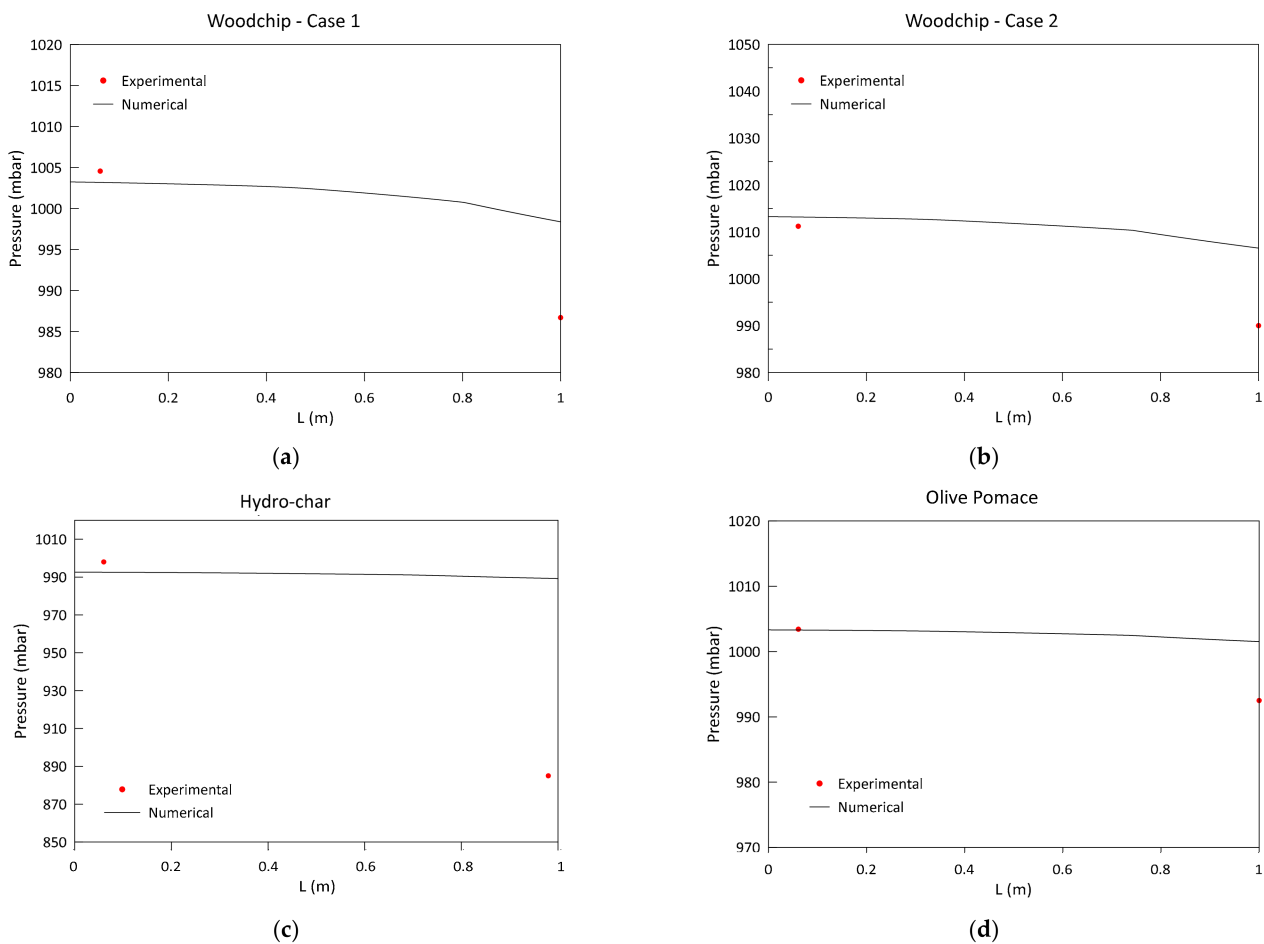
Figure 3. Comparison between the experimental measurements and the numerical temperature profile for the four biomasses/residual materials tested: (**a**) woodchip case 1, (**b**) woodchip case 2, (**c**) hydro-char from green waste, (**d**) olive pomace.

Figure 4. *Cont.*

(c)   (d)
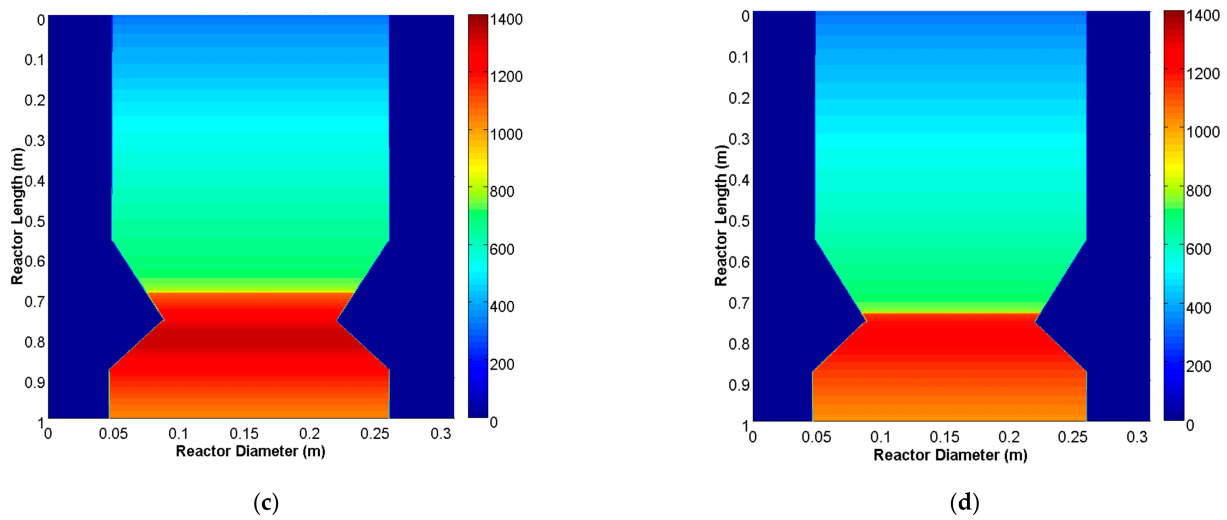
Figure 4. Numerical temperature profile (expressed in Kelvin) along the reactor axis for the four biomasses tested: (**a**) woodchip case 1, (**b**) woodchip case 2, (**c**) hydro-char from green waste, (**d**) olive pomace.

(a)   (b)

(c)   (d)

Figure 5. Comparison between the experimental measurements and the numerical pressure profiles for the four biomasses tested: (**a**) woodchip case 1, (**b**) woodchip case 2, (**c**) hydro-char from green waste, (**d**) olive pomace.

Figure 6 shows the evolution of the solid and gaseous species along the reactor axis. These trends exhibit a qualitatively identical profile for all the different biomasses, where the main differences occur in their values and in their positions along the reactor axis of the

combustion/gasification phases (the latter, however, is clearly marked by the temperature peak reported in Figure 3). Therefore, for the sake of brevity, they are shown only for the operative Case 1 of woodchip gasification.
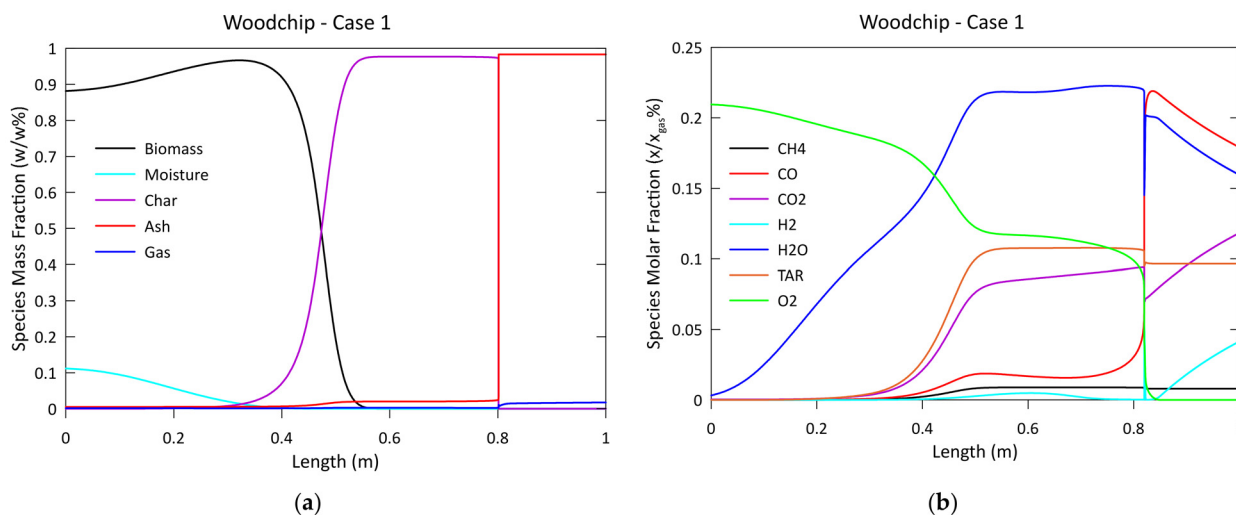
Figure 6. Numerical results on woodchip case 1 regarding the evolution of the mass fractions of the (**a**) solid and (**b**) gaseous species.

Figure 6a reports the mass fractions of the solid species (biomass, moisture, char and ashes) calculated with respect to the feedstock flowrate entering the gasifier. The biomass moisture content shown in Figure 6a rapidly goes to zero in the upper zone of the reactor where drying occurs; consequently, the complementary mass fraction relative to the biomass organic matter simultaneously increases. At the same time, the water vapor mass fraction, represented by the Gas line in Figure 6a and better shown in Figure 6b (where the species molar fractions are, instead, plotted and calculated with respect to the flowrate of only the gaseous species, this being the sum of the entering air and the gasification products), also increases. Nitrogen evolution in Figure 6b is not reported for the sake of clarity.

When temperature reaches 400 K at an axial position of around 0.35 m, devolatilization reactions occur. The mass fraction of the biomass organic matter decreases (Figure 6a), being completely converted into char and into permanent and condensable gases (Figure 6b) such as CO, CO_2, CH_4, H_2O, H_2 and tar.

After the pyrolysis reactions completely convert the organic matter into char and gaseous species, the constant trend depicted in the char mass fraction in Figure 6a corresponds to the distance required for the temperature to increase and activate the kinetic rate associated with the char oxidation.

Indeed, when the char begins to be oxidized, the O_2 decreases because of the gasification reactions of char reported in Equations (32)–(35), which lead to the production of CO, H_2 and CH_4. Simultaneously, these species further react with oxygen, to be oxidized into water vapour and carbon dioxide, as expressed in Equations (27)–(31). In this phase, the temperature witnesses a strong increase due to the exothermic nature of the oxidation reactions. At the end of the reduction stage, when the temperature reaches its peak and begins to show a negative slope, all chemical reactions are frozen except for the water–gas shift reaction (Equation (31)), which slightly favours the formation of CO_2 in the place of CO, as can be seen in the last part of Figure 6b.

A comparison between the measured and calculated mass fractions produced at the end of the gasification process is reported in Figure 7. The numerical and experimental results can be said to be in quite a good agreement, considering the complexity of the formulated numerical model, where a multiphase reacting flow is modelled within a 1D schematization. The best results are achieved for both of the woodchip gasification cases,

where the error between the measured and numerical values is equal to 12% in terms of the prediction of the CO and CO_2 species.
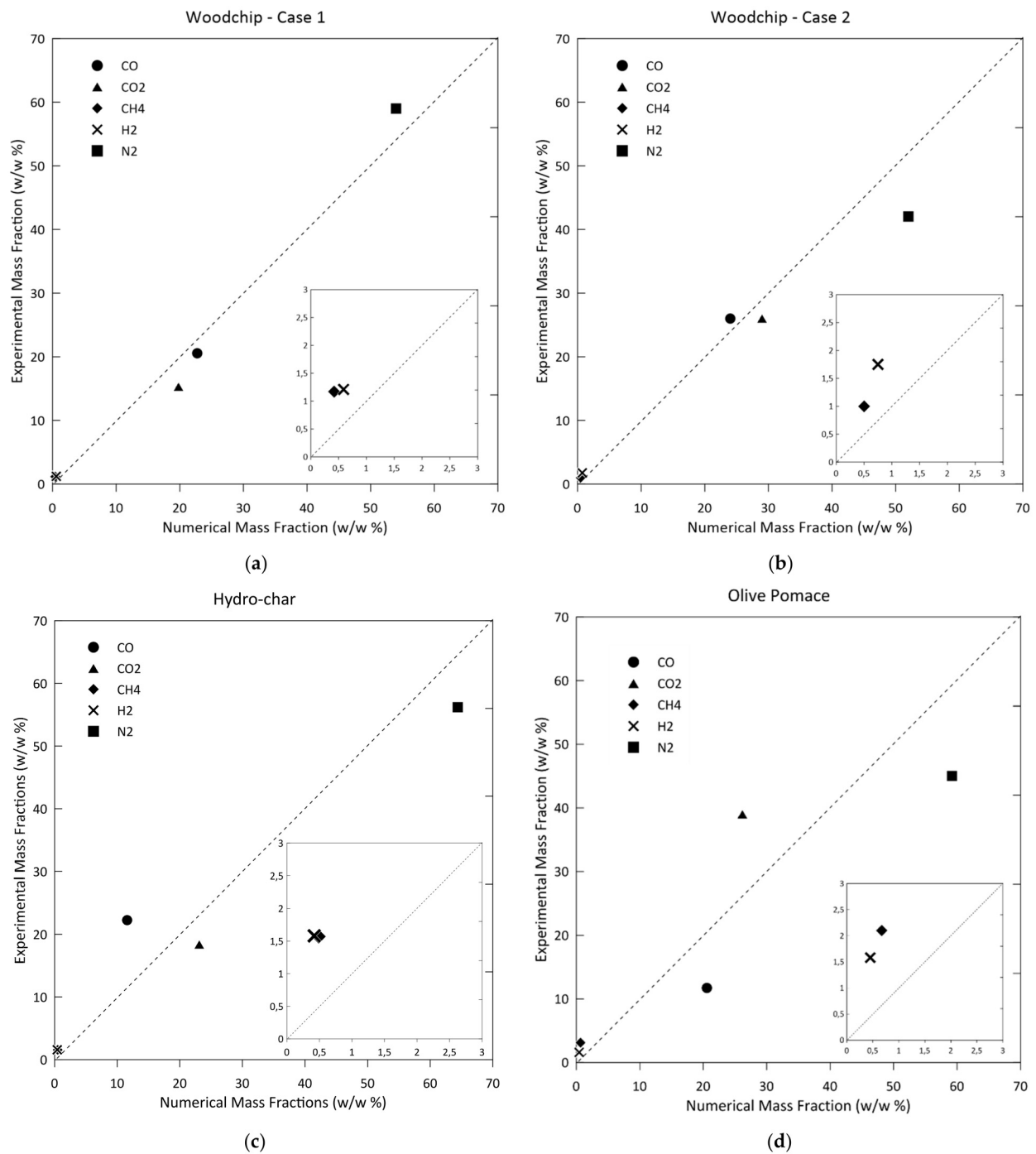

Figure 7. Linear adjustment comparison between the measured and numerical syngas species (on a dry tar-free basis) for the four biomasses tested: (**a**) woodchip case 1, (**b**) woodchip case 2, (**c**) hydro-char from green waste, (**d**) olive pomace.

A numerical underestimation of the CO species and an overestimation of the CO_2 is noticed for the operative case of hydro-char gasification. This can be explained by the influence of the temperature over the water–gas shift reaction kinetics, where a shift towards the CO_2 product is favoured at the highest temperatures reached in this operative case.

Moreover, a numerical underestimation of H_2 and CH4 species is evident for all the cases analysed. This gap can be explained by looking at Figure 6b, where it is evident that

the adopted gasification kinetics P3 ($C + H_2O = CO + H_2$) and P4 ($C + 2H_2 = CH_4$), reported in Equations (34) and (35), do not contribute any substantial increase in the production of these two species after the devolatilization phase. This aspect reveals how the gasification kinetics are well-balanced with the oxidation kinetics G2 ($H_2 + 1/2O_2 \rightarrow H_2O$) and G3 ($CH_4 + 2O_2 \rightarrow CO_2 + 2H_2O$) reported in Equations (28) and (29).

The underestimation of the CH_4 and H_2 species strongly affects the prediction of the syngas Lower Heating Value (LHV), as shown in Figure 8, especially for the hydro-char case, where the CO mass fraction is also not well predicted.
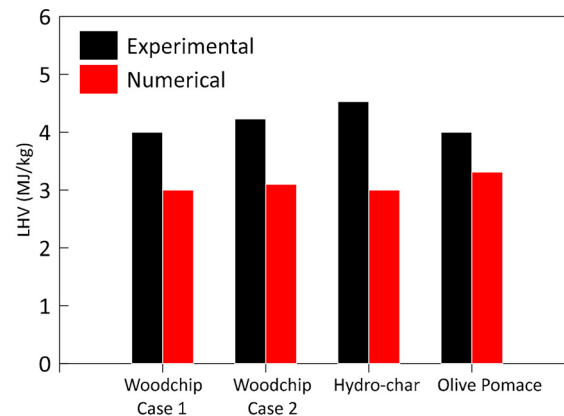
Figure 8. Histogram comparison between the measured and numerical syngas LHV for the four biomasses/residual materials tested.

3.2. Parametric Analysis of the Influence of the Gasification ER

The influence of the gasification ER on the gasification conversion efficiency is studied in the present section. Due to the similarity between the two woodchip biomass cases, the following analyses are performed just for the first case. Besides the operative ER of 0.3 assumed in the previous validation process, this parameter is here also considered as equal to 0.25 and 0.35. Figure 9 shows the evolution of gaseous temperature along the reactor axis. An increase in this parameter, due to an increase in the gasifying air mass flow rate, enhances the temperature peak by over 150 degrees. This phenomenon is a direct consequence of the operative condition present near the point of stoichiometric combustion, where a reduction in the syngas calorific value (as shown later) and an increase in the temperature of the reduction zone occur.
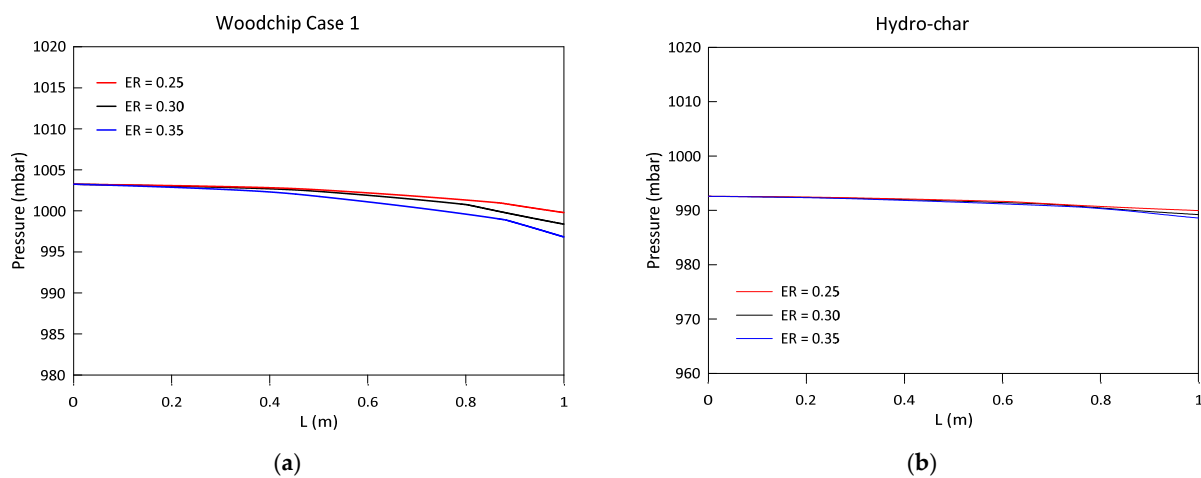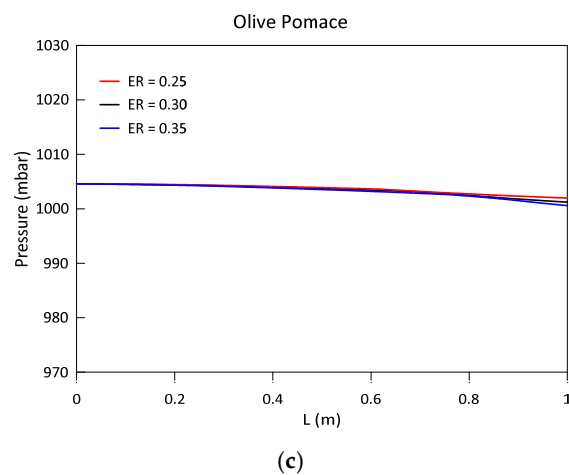

(**a**)

(**b**)

Figure 9. *Cont.*

(**c**)
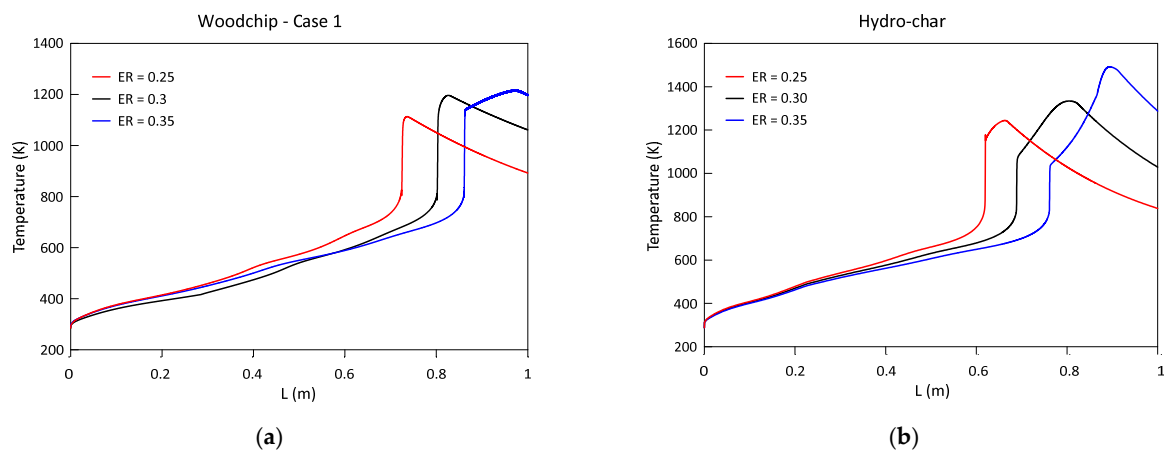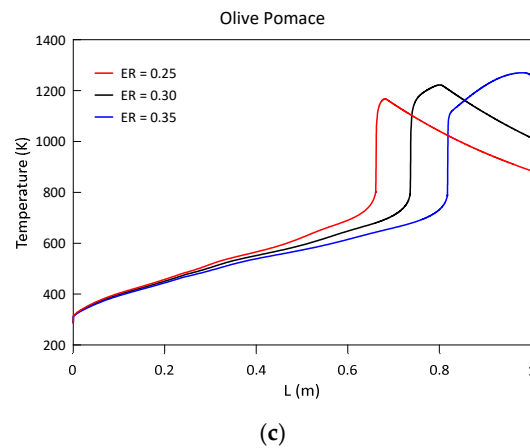
Figure 9. Temperature evolution along the reactor axis at different ER for (**a**) woodchip case 1, (**b**) hydro-char from green waste, (**c**) olive pomace.

It is also interesting to note that the reduction zone moves towards the reactor outlet section: this behaviour is physically explainable due to an increase in the quantity of oxygen in the air, which influences the effectiveness of the pyrolysis phase (or devolatization), with a consequent delay in the subsequent processes. On the other hand, it can be seen that the influence of this parameter on the gaseous pressure evolution shown in Figure 10 can be considered as negligible, as the maximum percentual variation occurring at the reactor section is equal to the 0.5% for the woodchip case. The variation with ER of the syngas species at the exit section of the gasifier is shown in Figure 11. The mass fractions are reported on a daf basis. An increase in the ER is associated with a decrease in CH_4 and H_2, as the operative conditions approach the stoichiometric ones. In the extreme case of ER = 1, a complete combustion and, consequently, a total consumption of the gaseous species H_2 and CH_4 occur. As concerns the CO, an increase in the ER shifts the reduction phase towards the reactor exit section (Figure 9), thus retarding the water–gas shift reaction which, in turn, favours the oxidation of this species to form CO_2 [43]. The lower calorific value (LHV) of the syngas therefore decreases, as shown in Figure 12; this is also due to an increase in the quantity of N_2 in the reactor, with a consequent decrease in the conversion efficiency.
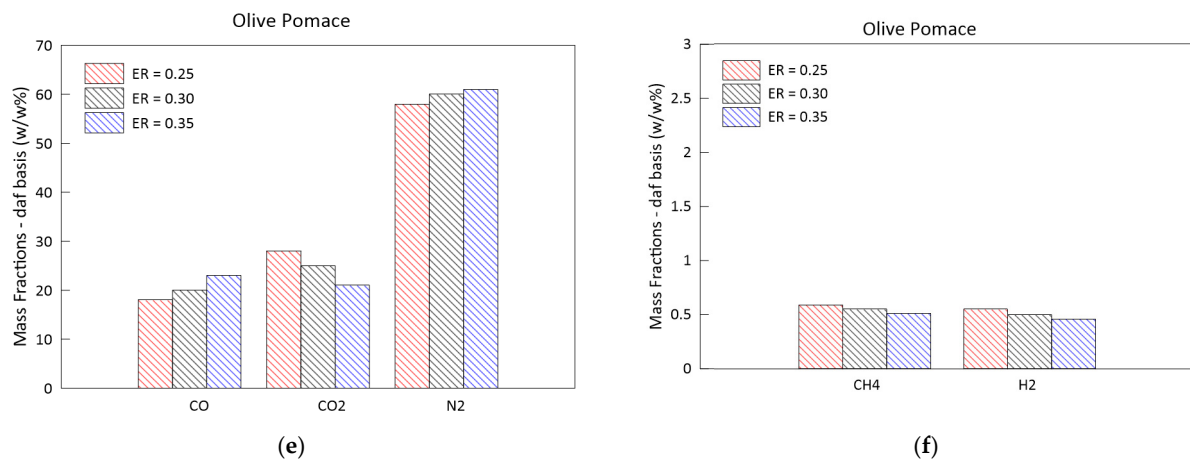

(**a**)
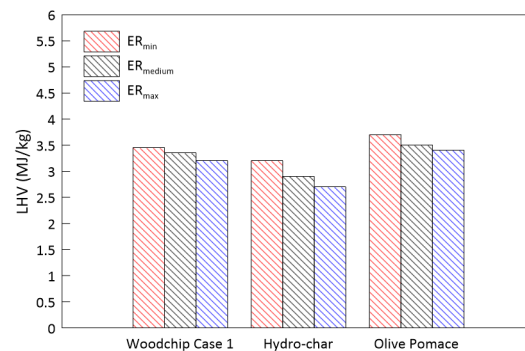

(**b**)

Figure 10. *Cont.*

(**c**)

Figure 10. Pressure evolution along the reactor axis at different ER for (**a**) woodchip case 1, (**b**) hydro-char from green waste, (**c**) olive pomace.

(**a**)

(**b**)

(**c**)

(**d**)
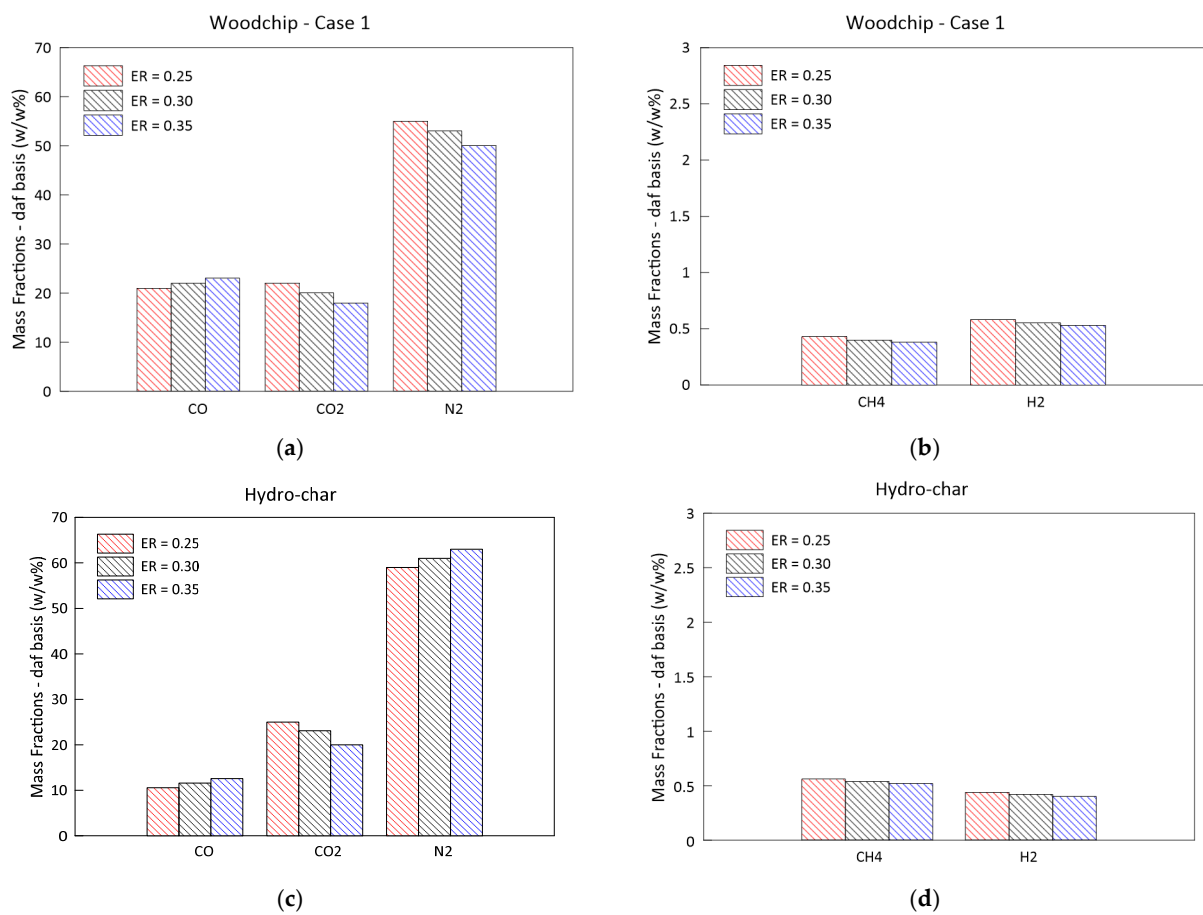
Figure 11. *Cont.*

Figure 11. Species mass fractions (on a daf basis) at the reactor exit section, at different ER, for (**a**,**b**) woodchip case 1, (**c**,**d**) hydro-char from green waste, (**e**,**f**) olive pomace gasification.


Figure 12. Syngas LHV (on a daf basis) at different ER for woodchip case 1, hydro-char from green waste, olive pomace.

3.3. Parametric Analysis of the Influence of the Bed Porosity

This parameter expresses the ratio between the volume not occupied by the raw material and the total volume; therefore, it is an expression of the degree of packaging of the solid material and of the consequent load losses that result from the process.

The degree of vacuum is a variable that affects all the non-ordinary differential equations of the system that is referred to as the gas phase, as shown in Equations (6)–(14) and (16), but it especially affects the pressure evolution as expressed by Equation (23), in which this parameter has an influence to the cubic power. Differently from the previously described results, where a default value of 0.5 is assumed (or 0.55 for the hydro-char case), this parameter is here also considered equal to 0.3 and 0.4 (0.35 and 0.45 for the hydro-char case) [44]. Figure 13 shows the evolution of the gaseous temperature for the three tested biomasses/residual materials. A decrease in the parameter indicates a greater raw material density along the reactor, thus determining a more delayed evolution of the drying, pyrolysis, combustion and gasification reactions. The greatest influence on the temperature peak value is noted for hydro-char case. As expected, the influence of this parameter on the gaseous pressure evolution shown in Figure 14 is decisive, since greater packaging (a lower value of the parameter ε) determines greater pressure losses along the reactor. Finally, the variation of the mass fractions of the gaseous species characterizing the syngas is reported in Figure 15. A greater degree of packaging (lower value of ε) corresponds with an increase in the percentage of CO and a decrease in CO_2, except in the woodchip case. In fact, as already mentioned, this parameter causes a greater delay in the evolution of the gasification and combustion reactions, and consequently, in the effectiveness of the water–gas shift reaction, which has a decisive role downstream of these reactions, inhibiting the conversion
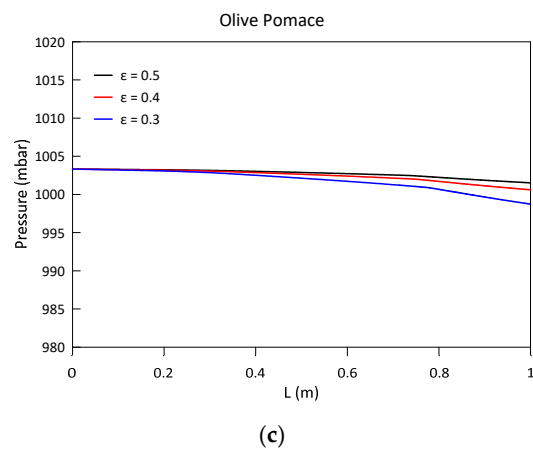
of CO to CO_2. Moreover, a slight reduction also occurs in the hydrogen mass fraction, with an overall effect of slightly reducing the syngas calorific value. This is shown in Figure 16.
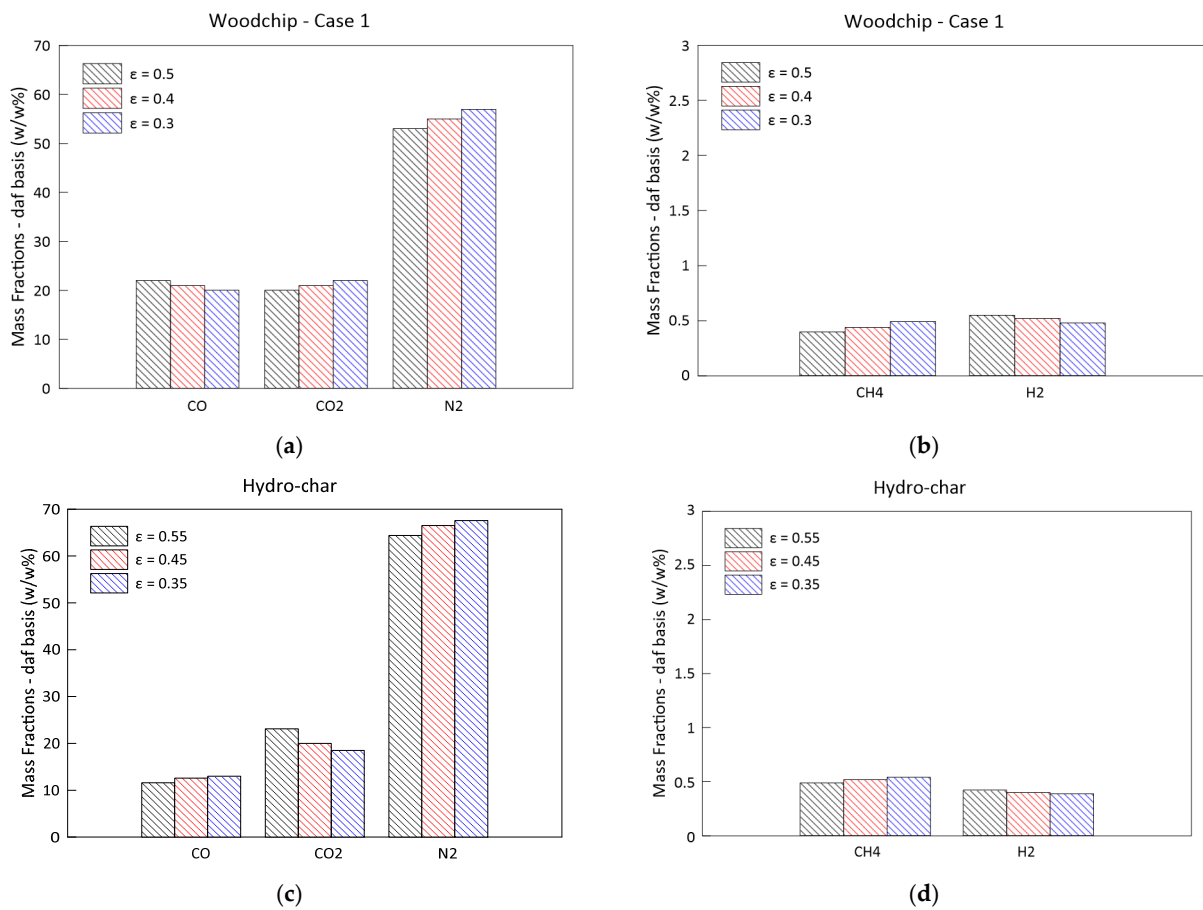

(a)

(b)

(c)
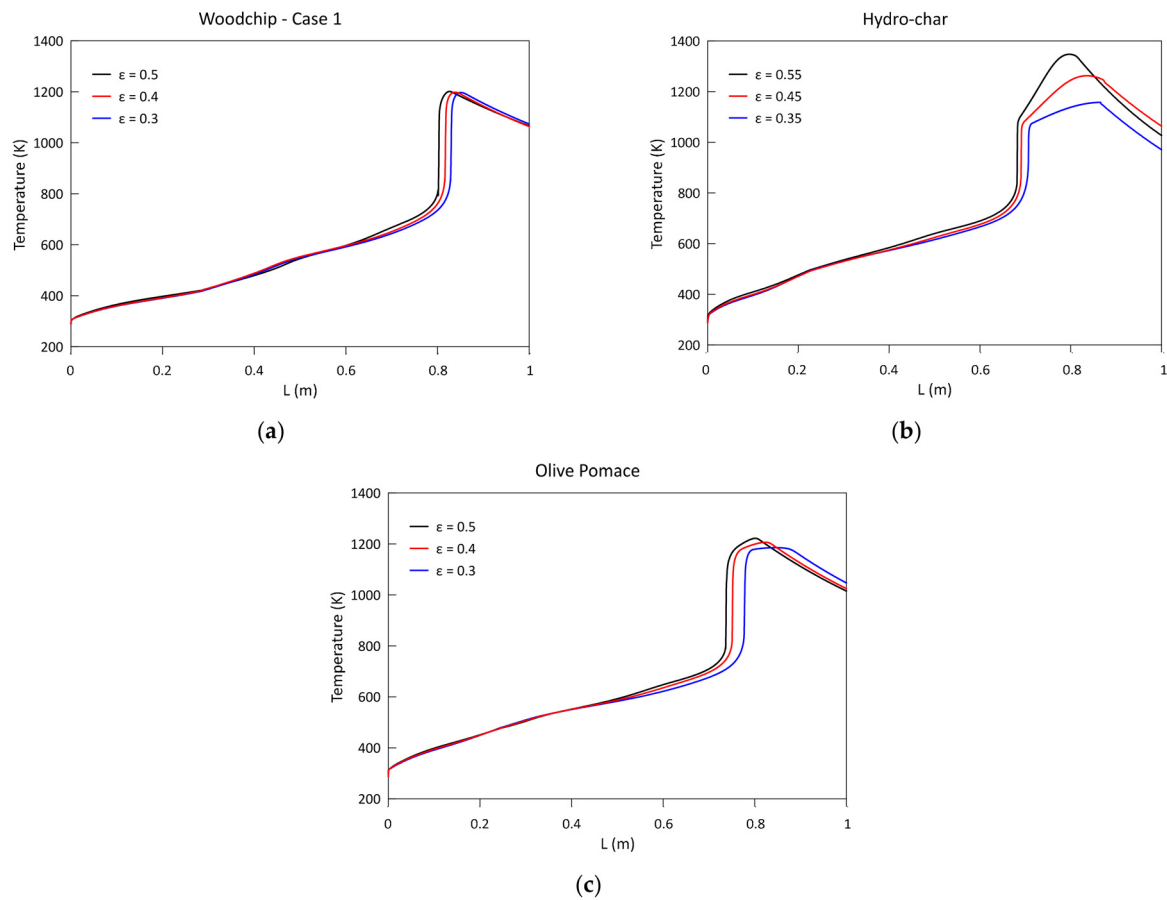
Figure 13. Temperature evolution along the reactor axis at different ε for (**a**) woodchip case 1, (**b**) hydro-char from green waste, (**c**) olive pomace.
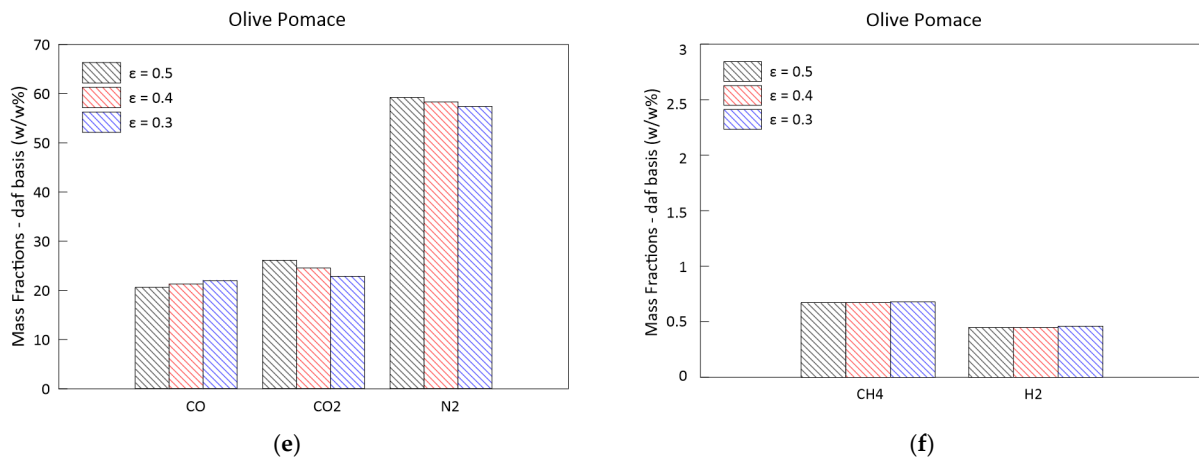

(a)

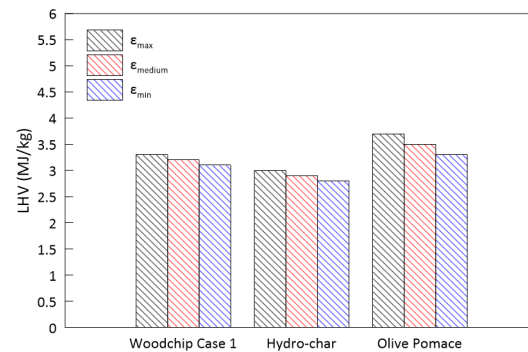(b)

Figure 14. *Cont.*

(**c**)
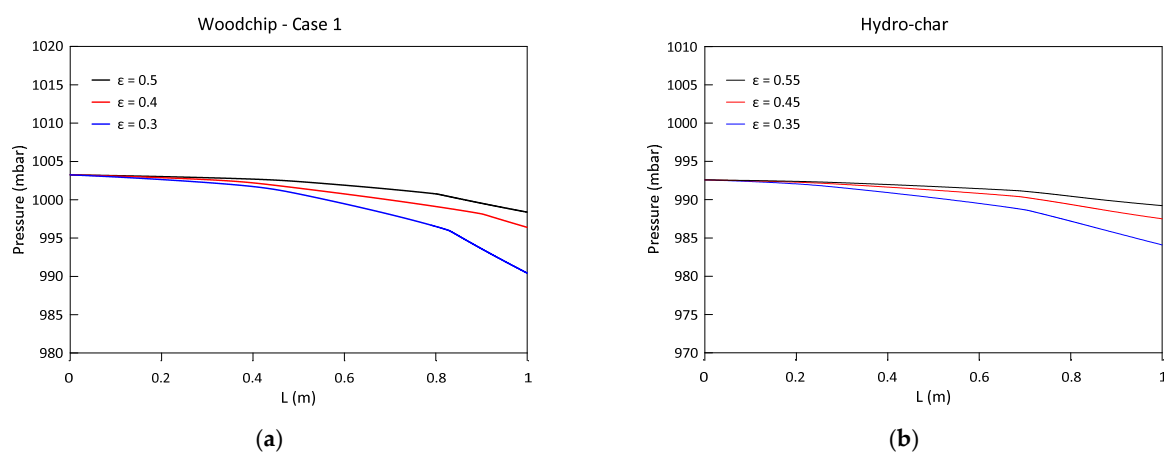
Figure 14. Pressure evolution along the reactor axis at different ε for (**a**) woodchip case 1, (**b**) hydro-char from green waste, (**c**) olive pomace.

(**a**)

(**b**)

(**c**)

(**d**)

Figure 15. *Cont.*

(e)

(f)

Figure 15. Species mass fractions (on a daf basis) at the reactor exit section, at different ε, for (**a**,**b**) woodchip case 1, (**c**,**d**) hydro-char from green waste, (**e**,**f**) olive pomace gasification.


Figure 16. Syngas LHV (on a daf basis) at different ε for woodchip case 1, hydro-char from green waste, olive pomace.

3.4. Parametric Analysis of the Biomass Moisture Content

The influence of the biomass moisture content is here investigated by considering a variation of this parameter of $\pm 5\%$ with respect to the initial value reported in Table 6. As shown in Figure 17, an increase in this parameter is associated with a delayed evolution of the temperature profile, as greater energy is spent during the evaporation process of the moisture content in the raw material before the subsequent pyrolysis, combustion and gasification phases take place. In fact, this phenomenon determines higher temperature values along the reactor for lower values of initial moisture contained. The pressure evolution is instead influenced in a negligible way, as shown in Figure 18.

The influence over the gaseous species that characterizes the syngas is shown in Figure 19, where an increase in the initial moisture content determines a slight increase in H_2 and CO_2 mass fraction and a decrease in CO. Methane, on the other hand, shows contrasting trends in the case of olive pomace with respect to the others, as its mass fraction reduces as the moisture content increases. As a global effect, a lower syngas calorific value is achieved, as shown in Figure 20, which can be explained through a reduction in the effectiveness of each reaction taking place after the drying phase, especially the water–gas shift reaction that determines a greater consumption of the CO species in favor of the production of hydrogen and CO_2 [9].
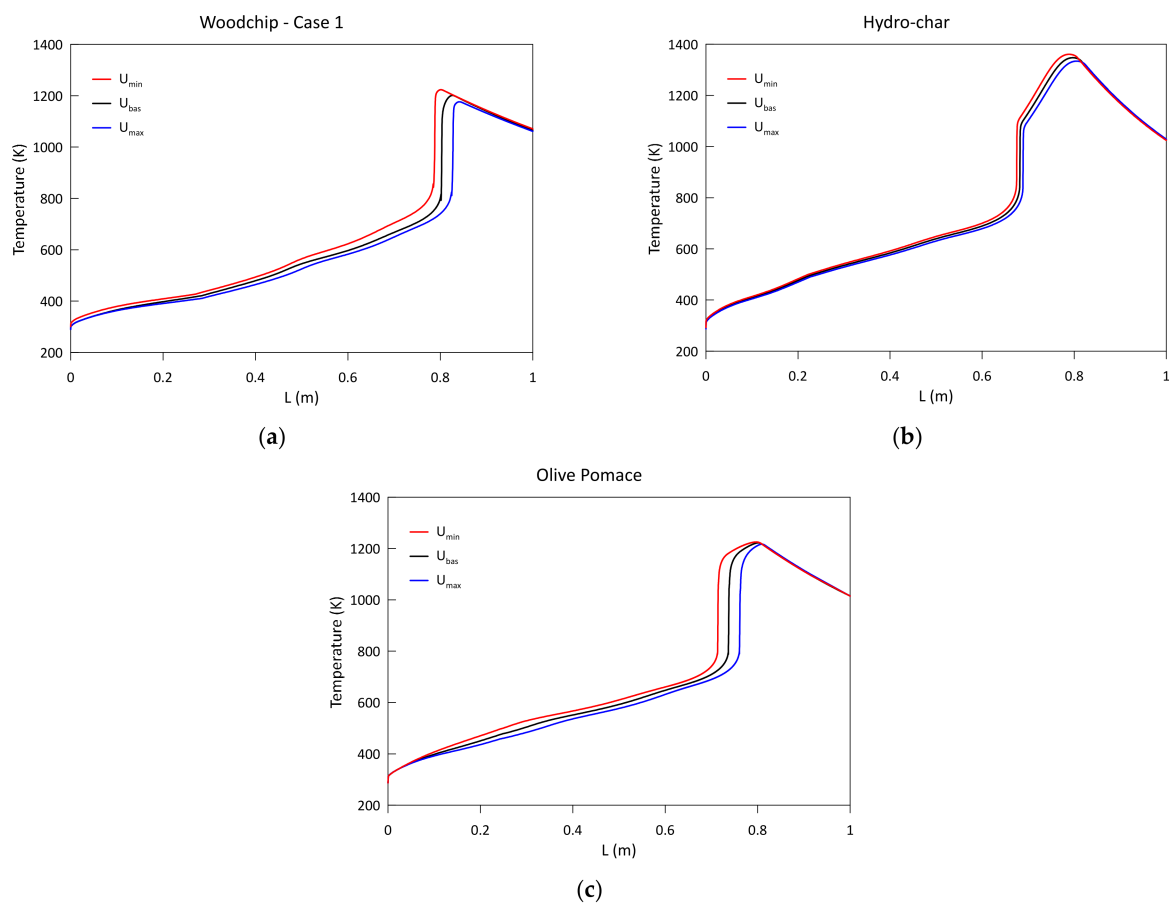
Figure 17. Temperature evolution along the reactor axis at different biomass/residual material initial moisture content levels for (**a**) woodchip case 1, (**b**) hydro-char from green waste, (**c**) olive pomace.

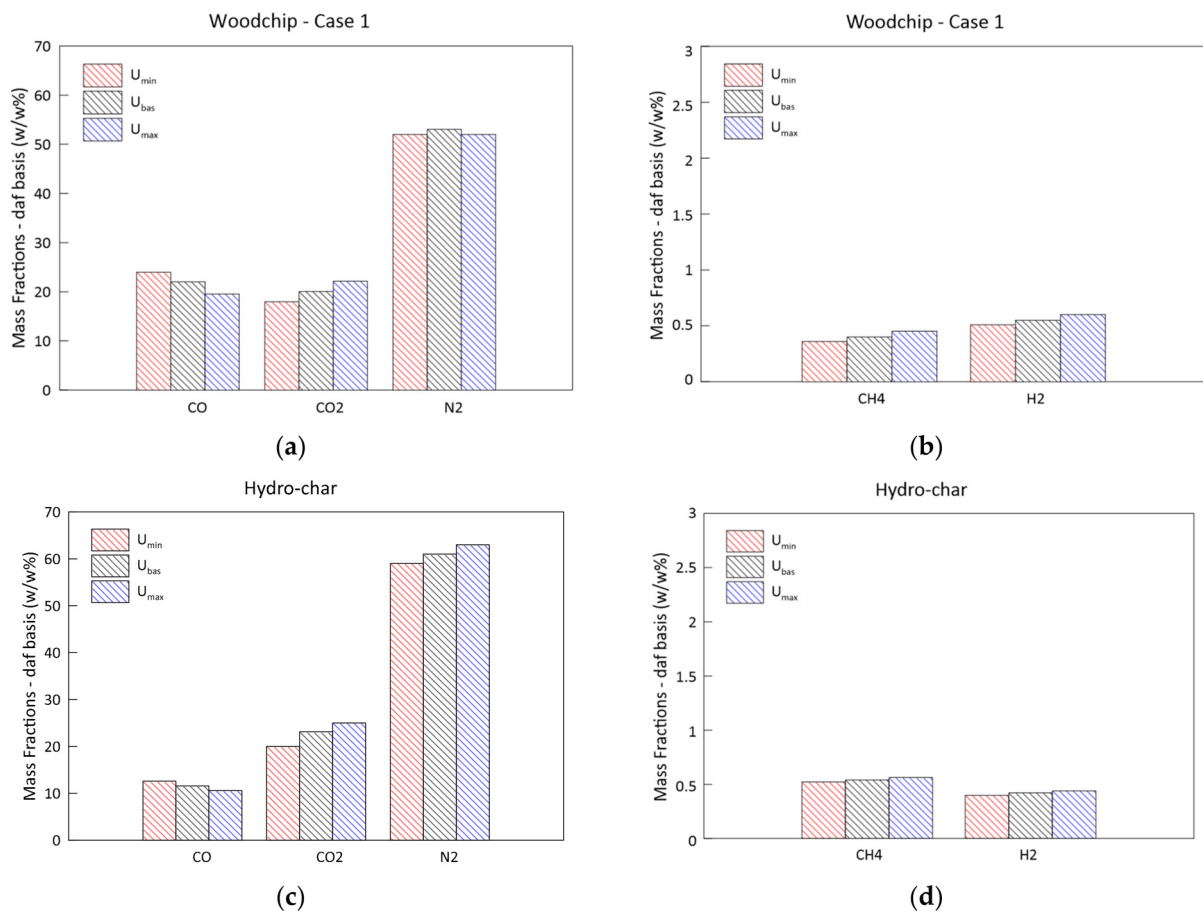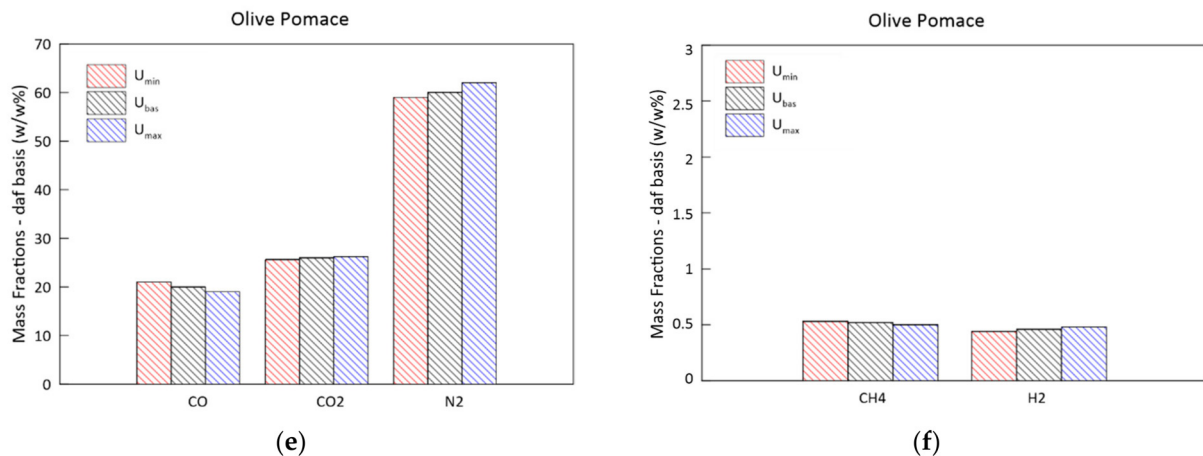**Figure 18.** *Cont.*

(**c**)
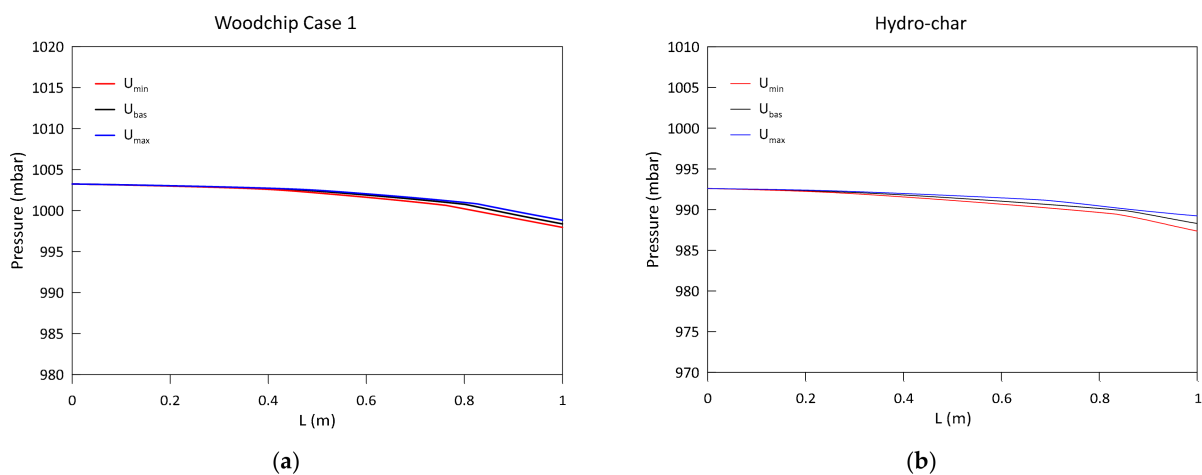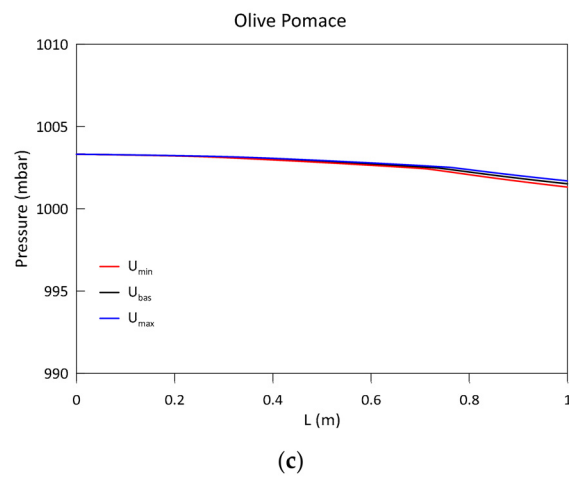
Figure 18. Pressure evolution along the reactor axis at different biomass/residual material initial moisture content levels for (**a**) woodchip case 1, (**b**) hydro-char from green waste, (**c**) olive pomace.

(**a**)

(**b**)

(**c**)

(**d**)

Figure 19. *Cont*.

(**e**)　　　(**f**)

Figure 19. Species mass fractions (on a daf basis) at the reactor exit section for (**a**,**b**) woodchip case 1, (**c**,**d**) hydro-char from green waste, (**e**,**f**) olive pomace gasification at different biomass/residual material initial moisture content levels.

Figure 20. Syngas LHV (on a daf basis) at different biomass/residual material initial moisture content levels for woodchip case 1, hydro-char from green waste, olive pomace.
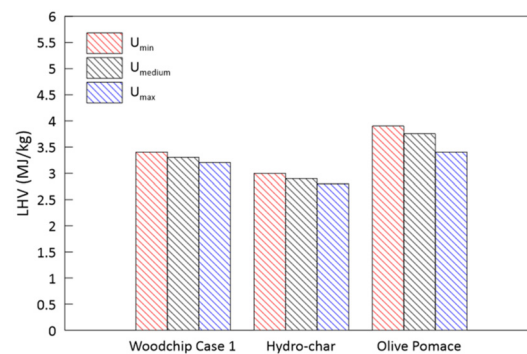
4. Conclusions

A flexible stationary phenomenological 1D model of biomass gasification is presented with reference to a real gasifier being part of a micro-cogeneration system. The most critical points of the proposed formulation, namely the limits of the assumed thermochemical conversion kinetics, are highlighted when applied to materials of different origins: two different typologies of woodchips, hydro-char from green waste, and briquettes of olive pomace and sawdust are considered. Their composition, degree of porosity and flowrates are experimentally measured at the plant site for a correct model initialization.

The evolution and order of magnitude of temperature along the reactor gasifier is well respected as the biomass varies, registering a temperature peak of 1345 K for the hydro-char case compared to a value of around 1200 K of the other raw materials because of the densified char having the highest heating value.

However, the measured pressure drop of about 80 mbar is underestimated by the numerical results due to the SP approach adopted. Moreover, the species composing the producer gas evaluated at the exit section of the reactor are found to be in quite good agreement with the measurements, especially for the woodchip cases, although an underestimation of the species CH_4 and H_2 is noticed for all the investigated cases.

Lastly, the parametric study of the influence of different operative parameters, such as ER, bed porosity and biomass moisture content, on the gasification efficiency, revealed that:

- Higher ERs lead to syngas characterized by a lower heating values and to higher temperatures achieved in the reduction zone;
- A greater biomass packaging in the reactor determines a general shift of reactivity towards the exit section: the greatest influence can be noticed on the pressure drop

along the reactor axis. The delay in the combustion and gasification reactions also causes a reduction in CH_4 and H_2;

- An increase in the biomass moisture content delays the evolution of the temperature profile, as greater energy is spent during the evaporation process. This also occurs at the expense of the H_2 and CH_4 produced in the subsequent phases, resulting in a syngas of poorer quality. The pressure evolution is instead influenced in a negligible way.

In summary, the present work is intended to provide a valuable basis upon which, following subsequent integration with additional kinetics, a more accurate prediction of system performance may be possible in cases when non-woody materials are used.

Supplementary Materials: The following are available online at https://www.mdpi.com/article/10.3390/en14144226/s1, Table S1: Devolatilization products kinetic rates used within the present model, Table S2: Kinetic constants used in the present model [22].

Author Contributions: Conceptualization, M.C., M.L.V. and D.P.; methodology, M.C., M.L.V. and D.P.; software, M.C., M.L.V. and D.P.; validation, M.C., M.L.V. and D.P.; formal analysis, M.C., M.L.V. and D.P.; investigation, M.C., M.L.V. and D.C.; resources, M.C., M.L.V. and D.C.; data curation, D.P.; writing—original draft preparation, M.L.V. and D.P.; writing—review and editing, M.C., M.L.V. and D.P.; visualization, D.P.; supervision, M.C. and D.C. All authors have read and agreed to the published version of the manuscript.

Conflicts of Interest: The authors declare no conflict of interest. The funders had no role in the design of the study; in the collection, analyses, or interpretation of data; in the writing of the manuscript, or in the decision to publish the results.

Nomenclature

Latin symbol	*Quantity and SI Unit*
1D	Mono Dimensional
a, b, c, d, e, f, g, m, n	Stoichiometric coefficient gas phase for N_2, H_2O, CO_2, CO, H_2, CH_4, H_2S, C_mH_n
A	Ash
A_{H_2O}	Pre-exponential factor of the drying reaction—s^{-1}
A_{SG}	Specific surface area of the particle—$m^2\,m^{-3}$
C	Char
CHP	Combined Heat and Power
CH_4	Methane
CO	Carbon monoxide
CO_2	Carbon dioxide
C_mH_n	Tar
cp_{Gj}	Specific heat gas for j = O_2 , N_2, H_2O, CO, CO_2, H_2, CH_4, H_2S, C_mH_n—$J\,kg^{-1}K^{-1}$
cp_{Si}	Specific heat solid for i = Wood Daf_{SS}, Moisture, Char, Ash —$J\,kg^{-1}K^{-1}$
D_i	Species Diffusivity Coefficient—$m^2\,s^{-1}$
D_{react}	Reactor Diameter—m
d_{p0}	Particle diameter—m
d_c	Inner core diameter—m
ER	Equivalence Ratio

M	Moisture
M_C	Molecular weight Char—kg kmol^{-1}
M_j	Molecular weight gas species for j = O_2 , N_2, H_2O, CO, CO_2, H_2, CH_4, H_2S, C_mH_n— kg kmol^{-1}
N_2	Nitrogen
GHG	Green House Gases
H_2	Hydrogen
H_2O	Vapour water
H_2S	Hydrogen sulfide
H_{Gj}	Gas enthalpy for j = O_2 , N_2, H_2O, CO, CO_2, H_2, CH_4, H_2S, C_mH_n— J kg^{-1}
H_{Si}	Solid enthalpy for i = Wood Daf$_{SS}$, Moisture, Char, Ash— J kg^{-1}
h_{SG}	Coefficient of solid-gas heat exchange—W m^{-2} K^{-1}
h_{GW}	Coefficient of gas-wall heat exchange—W m^{-2} K^{-1}
h_{SW}	Coefficient of solid-wall heat exchange—W m^{-2} K^{-1}
k_G	Kinetic constant for homogeneous reactions gas phase— m s^{-1}
$k_{ash,Gl}$	Ash film diffusion constant for Gl = O_2, CO_2, H_2, H_2O— m s^{-1}
$k_{diff,Gl}$	Gas film diffusion constant for Gl = O_2, CO_2, H_2, H_2O— m s^{-1}
$k_{Rp,Gl}$	Kinetic constant for heterogeneous reactions for Gl = O_2, CO_2, H_2, H_2O—m s^{-1}
k_{wG}	Kinetic constant of the water gas shift reaction—m s^{-1} kmol^{-1}
K_0	Pre-exponential factor of the devolatilization reaction—s^{-1}
$K_{wG,eq}$	Equilibrium constant of the water gas shift reaction
LHV	Lower Heating Value
ODE	Ordinary Differential Equations
O_2	Oxygen
P	Total pressure—atm
Q_{GW}	Gas-wall heat exchanged—W m^{-3}
Q_{SG}	Solid-gas heat exchanged—W m^{-3}
Q_{SW}	Solid-wall heat exchanged—W m^{-3}
R	Universal gas constant—atm m^3 kmol^{-1} K^{-1}
R_{dev}	Reaction rate devolatilization—kg s^{-1} m^{-3}
R_{dry}	Reaction rate drying—kg s^{-1} m^{-3}
R_{Gl}	Reaction rate homogeneous reactions gas phase—kmol s^{-1} m^{-3}
R_{Sp}	Reaction rate heterogeneous reactions involving carbon—kg s^{-1} m^{-3}
SP	Shell progressive
T_G	Gas temperature—K
T_S	Solid temperature —K
T_{Wall}	Wall temperature —K
U_G	Gas velocity—m s^{-1}
U_S	Solid velocity—m s^{-1}
W_{daf}	Biomass/residual material (dry-ash free basis)
Greek symbol	*Quantity and SI Unit*
$\alpha 1$, $\beta 1$, $\gamma 1$, $\delta 1$, $\varepsilon 1$	Stoichiometric coefficient for raw material
$\alpha 2$	Stoichiometric coefficient gas phase for C
ΔH_{dry}	Heat of reaction water vapour—J kg^{-1}
$\Delta H_{R_{Gl}}$	Heat of reaction for homogeneous reactions gas phase—J kg^{-1}
$\Delta H_{R_{Sp}}$	Heat of reaction for heterogeneous reactions involving carbon —J kg^{-1}
ΔV	Differential volume—m^3
Δz	Height along the gasifier—m
ε	Degree of vacuum of the bed
ζ	Correction factor for solid-gas heat exchange coefficient
μ_G	Fluid viscosity—kg m^{-1}s^{-1}
η_i	Devolatilization yields

v_{jl}	Stoichiometric coefficient gas phase f for j = O_2, N_2, H_2O, CO_2, CO, H_2, C_mH_n
ξ	Fraction of the particle radius occupied by unreacted char
ρ_i	Solid partial bed densities for i = $Wdaf_{SS}$, M, C and A—kg m^{-3}
ρ_j	Gas phase partial densities for j = O_2, N_2, H_2O, CO_2, CO, H_2, CH_4, H_2S, C_mH_n—kg m^{-3}
Subscripts and superscripts	***Quantity and SI Unit***
ash	Referred to ash
C	Referred to char
dev	Referred to devolatilization
diff	Referred to diffusion
dry	Referred to drying
G	Referred to gas
G1,2,3,4	Referred to gas homogeneous reactions gas phase
Gl	Referred to gas species O_2, CO_2, H_2, H_2O
Gj	Referred to gas species j = O_2, N_2, H_2O, CO, CO_2, H_2, CH_4, H_2S, C_mH_n
P	Referred to particle
R	Referred to reaction
S	Referred to solid
Si	Referred to solid species i = Wood Daf_{SS}, Moisture, Char, Ash
Sp1,2,3,4	Referred to heterogeneous reactions involving carbon
GW	Referred to gas-wall
SG	Referred to solid-gas
SW	Referred to solid-wall
W	Referred to wall
WG	Referred to water gas shift reaction

References

1. IRENA: Global Energy Transformation, A Roadmap to 2050. Available online: https://www.irena.org/media/Files/IRENA/Agency/Publication/2018/Apr/IRENA_Report_GET_2018.pdf (accessed on 10 February 2021).
2. IEA International Energy Agency, Renewables 2019—Analysis and Forecast to 2024. Available online: https://webstore.iea.org/market-report-series-renewables-2019 (accessed on 10 January 2021).
3. Costa, M.; Buono, A.; Caputo, C.; Carotenuto, A.; Cirillo, D.; Costagliola, M.A.; Di Blasio, G.; La Villetta, M.; Macaluso, A.; Martoriello, G.; et al. The "INNOVARE" Project: Innovative Plants for Distributed Poly-Generation by Residual Biomass. *Energies* **2020**, *13*, 4020. [CrossRef]
4. Vassilev, S.V.; Vassileva, C.G.; Vassilev, V.S. Advantages and disadvantages of composition and properties of biomass in comparison with coal: An overview. *Fuel* **2015**, *158*, 330–350. [CrossRef]
5. Guo, F.; Dong, Y.; Dong, L.; Guo, C. Effect of design and operating parameters on the gasification process of biomass in a downdraft fixed bed: An experimental study. *Int. J. Hydrog. Energy* **2014**, *39*, 5625–5633. [CrossRef]
6. Palma, C.F. Modelling of tar formation and evolution for biomass gasification: A review. *Appl. Energy* **2013**, *111*, 129–141. [CrossRef]
7. Trninić, M.; Stojiljković, D.; Manić, N.; Skreiberg, Ø.; Wang, L.; Jovović, A. A mathematical model of biomass downdraft gasification with an integrated pyrolysis model. *Fuel* **2020**, *265*, 116867. [CrossRef]
8. Basu, P. *Biomass Gasification and Pyrolysis*; Elsevier: New York, NY, USA, 2010.
9. La Villetta, M.; Costa, M.; Massarotti, N. Modelling approaches to biomass gasification: A review with emphasis on the stoichiometric method. *Renew. Sustain. Energy Rev.* **2017**, *74*, 71–88. [CrossRef]
10. Adeyemi, I.; Janajreh, I.; Arink, T.; Ghenai, C. Gasification behavior of coal and woody biomass: Validation and parametrical study. *Appl. Energy* **2017**, *185*, 1007–1018. [CrossRef]
11. Giltrap, D.; McKibbin, R.; Barnes, G. A steady state model of gas-char reactions in a downdraft biomass gasifier. *Sol. Energy* **2003**, *74*, 85–91. [CrossRef]
12. Wang, Y.; Kinoshita, C. Kinetic model of biomass gasification. *Sol. Energy* **1993**, *51*, 19–25. [CrossRef]
13. Di Blasi, C. Dynamic behaviour of stratified downdraft gasifiers. *Chem. Eng. Sci.* **2000**, *55*, 2931–2944. [CrossRef]
14. Sharma, A.K. Equilibrium and kinetic modeling of char reduction reactions in a downdraft biomass gasifier: A comparison. *Sol. Energy* **2008**, *82*, 918–928. [CrossRef]
15. Tinaut, F.; Melgar, A.; Pérez, J.F.; Horrillo, A. Effect of biomass particle size and air superficial velocity on the gasification process in a downdraft fixed bed gasifier. An experimental and modelling study. *Fuel Process. Technol.* **2008**, *89*, 1076–1089. [CrossRef]
16. Umeki, K.; Namioka, T.; Yoshikawa, K. Analysis of an updraft biomass gasifier with high temperature steam using a numerical model. *Appl. Energy* **2012**, *90*, 38–45. [CrossRef]

17. Simone, M.; Nicolella, C.; Tognotti, L. Numerical and experimental investigation of downdraft gasification of woody residues. *Bioresour. Technol.* **2013**, *133*, 92–101. [CrossRef]
18. Patra, T.K.; Nimisha, K.; Sheth, P.N. A comprehensive dynamic model for downdraft gasifier using heat and mass transport coupled with reaction kinetics. *Energy* **2016**, *116*, 1230–1242. [CrossRef]
19. Salem, A.M.; Paul, M.C. An integrated kinetic model for downdraft gasifier based on a novel approach that optimises the reduction zone of gasifier. *Biomass Bioenergy* **2018**, *109*, 172–181. [CrossRef]
20. Tartarelli, R.; Seggiani, M. Analisi e Modellazione Numerica del Processo di Gassificazione del Carbone in Reattori Updraft; ENEA 2010 Report RdS 27. Available online: https://www.enea.it/it/Ricerca_sviluppo/documenti/ricerca-di-sistema-elettrico/gassificazione-carbone/28-dicmpi-rt-5252-modgsf.pdf (accessed on 12 July 2021).
21. Knacke, O.; Kubaschewski, O.; Hesselmann, K. *Thermo-Chemical Properties of Inorganic Substances*, 2nd ed.; Springer: Berlin/Heidelberg, Germany, 1991.
22. Hobbs, M.L.; Radulovic, P.T.; Smoot, L.D. Modeling fixed-bed coal gasifiers. *AIChE J.* **1992**, *38*, 681–702. [CrossRef]
23. Mandl, C.; Obernberger, I.; Biedermann, F. Updraft fixed-bed gasification of softwood pellets: Mathematical modelling and comparison with experimental data. In Proceedings of the 17th European Biomass Conference & Exhibition, ETA-Renewable Energies, Hamburg, Germany, 29 June–3 July 2009.
24. Koufopanos, C.A.; Papayannanos, N.; Maschio, G.; Lucchesi, A. Modeling the pyrolysis of biomass particles: Studies on kinetics, thermal and heat transfer effects. *Can. J. Chem. Eng.* **1991**, *69*, 907–915. [CrossRef]
25. Chan, W.-C.R.; Kelbon, M.; Krieger, B.B. Modelling and experimental verification of physical and chemical processes during pyrolysis of a large biomass particle. *Fuel* **1985**, *64*, 1505–1513. [CrossRef]
26. Di Blasi, C.; Russo, G. *Modelling of Transport Phenomena and Kinetics of Biomass Pyrolysis, Advances in Thermochemical Biomass Conversion*; Springer: Berlin/Heidelberg, Germany, 1993; pp. 906–921. [CrossRef]
27. Font, R.; Marcilla, A.; Verdu, E.; Devesa, J. Kinetics of the pyrolysis of almond shells and almond shells impregnated with cobalt dichloride in a fluidized bed reactor and in a pyroprobe 100. *Ind. Eng. Chem. Res.* **1990**, *29*, 1846–1855. [CrossRef]
28. Janse, A.; Westerhout, R.; Prins, W. Modelling of flash pyrolysis of a single wood particle. *Chem. Eng. Process. Process Intensif.* **2000**, *39*, 239–252. [CrossRef]
29. Shafizadeh, F.; Chin, P.P.S. *Thermal Deterioration of Wood*; ACS Series American Chemical Society; ACS Publications: Washington, DC, USA, 1977; pp. 57–81. [CrossRef]
30. Thurner, F.; Mann, U. Kinetic investigation of wood pyrolysis. *Ind. Eng. Chem. Process. Des. Dev.* **1981**, *20*, 482–488. [CrossRef]
31. Bin Yang, Y.; Phan, A.N.; Ryu, C.; Sharifi, V.; Swithenbank, J. Mathematical modelling of slow pyrolysis of segregated solid wastes in a packed-bed pyrolyser. *Fuel* **2007**, *86*, 169–180. [CrossRef]
32. Ahmed, S.; Clements, L.D. Kinetics of Biomass Pyrolysis with Radiant Heating. In Proceedings of the International Conference on Research in Biomass Conversion, Phoenix, AZ, USA, 2 April 1988. [CrossRef]
33. Teislev, B. Simulation of the Biomass Updraft Gasifier, MEK-ET. 2006. Available online: http://www.risoe.dk/rispubl/NEI/mek-et-2006-02.pdf (accessed on 12 July 2021).
34. Molina, A.; Mondragón, F. Reactivity of coal gasification with steam and CO_2. *Fuel* **1998**, *77*, 1831–1839. [CrossRef]
35. Liliedahl, T.; Sjöström, K. Modelling of char-gas reaction kinetics. *Fuel* **1997**, *76*, 29–37. [CrossRef]
36. Kajitani, S.; Suzuki, N.; Ashizawa, M.; Hara, S. CO_2 gasification rate analysis of coal char in entrained flow coal gasifier. *Fuel* **2006**, *85*, 163–169. [CrossRef]
37. Ozbas, K.E.; Kök, M.V.; Hiçyilmaz, C. Comparative kinetic analysis of raw and cleaned coals. *J. Therm. Anal. Calorim.* **2002**, *69*, 541–549. [CrossRef]
38. Henrich, E.; Bürkle, S.; Meza-Renken, Z.; Rumpel, S. Combustion and gasification kinetics of pyrolysis chars from waste and biomass. *J. Anal. Appl. Pyrolysis* **1999**, *49*, 221–241. [CrossRef]
39. Scott, S.; Davidson, J.; Dennis, J.; Fennell, P.; Hayhurst, A. The rate of gasification by CO_2 of chars from waste. *Proc. Combust. Inst.* **2005**, *30*, 2151–2159. [CrossRef]
40. Yang, W.; Ponzio, A.; Lucas, C.; Blasiak, W. Performance analysis of a fixed-bed biomass gasifier using high-temperature air. *Fuel Process. Technol.* **2006**, *87*, 235–245. [CrossRef]
41. Costruzioni Motori Diesel (CMD). Pirogassificatore ECO20 X. Available online: http://www.cmdengine.com/eco20-pirogassificatore (accessed on 12 May 2020).
42. Costa, M.; Rocco, V.; Caputo, C.; Cirillo, D.; Di Blasio, G.; La Villetta, M.; Martoriello, G.; Tuccillo, R. Model based optimization of the control strategy of a gasifier coupled with a spark ignition engine in a biomass powered cogeneration system. *Appl. Therm. Eng.* **2019**, *160*, 114083. [CrossRef]
43. Costa, M.; La Villetta, M.; Massarotti, N. Optimal tuning of a thermo-chemical equilibrium model for downdraft biomass gasifiers. *Chem. Eng.* **2015**, *43*, 439–444. [CrossRef]
44. Wang, S.C.; Wen, C.Y. Experimental evaluation of nonisotheral solid-gas reaction model. *AIChE J.* **1972**, *18*, 1231–1238. [CrossRef]